

# Hadronic Dark Matter Searches at CMS at $\sqrt{s} = 13 \text{ TeV}$

Searches for invisibly decaying Higgs bosons and semi-visible jets

By

ESHWEN BHAL



SCHOOL OF PHYSICS  
UNIVERSITY OF BRISTOL

A dissertation submitted to the University of Bristol in accordance with the requirements for award of the degree of DOCTOR OF PHILOSOPHY in the Faculty of Science.

APRIL 2020

### Word count: number in words

Draft: 13th April 2020

**ABSTRACT**

<sup>17</sup> H ere goes the abstract

Draft: 13th April 2020

## DEDICATION AND ACKNOWLEDGEMENTS

19 This work is dedicated to my grandfather, Dato' Mahindar Singh Bhal, who was able  
20 to begin this journey with me but sadly unable to finish it. There are far too many  
21 people and too little space to individually thank everyone who has accompanied me  
22 during this PhD, but I'll try my best.

23 Firstly, to my supervisor, Dr. Henning Flächer. Your advice and guidance over the course  
24 of this degree has been instrumental to achieving it, as well as encouraging my growth as a  
25 researcher.

26 Secondly, to all my colleagues at the University of Bristol. Very little would have been  
27 achieved without your help. From scientific discussions in the pub to pub discussions in the  
28 physics building, they have all been fruitful either directly or by helping me detach from  
29 work. Special thanks are in order to Simone and Sam Maddrell-Mander in my cohort, who  
30 have put up with my complaining during the stressful times.

31 To my friends from Monmouth that include my best friends in the world, Mike, James,  
32 Sneddon, (Mini) Sam, and Matt Bristow. You've been on this adventure with me since our  
33 school days and had my back the entire time. We've been through the highest, lowest, and  
34 most hilarious times together. I can definitively say I would not be the person I am today  
35 without you.

36 To my friends from LTA and those based at CERN, especially Dwayne, Vukasin, and  
37 Matt Heath. You became my second family while I was in Geneva. I'll miss the skiing, trips  
38 into the city, games, and general banter.

39 To my undergraduate cohort from Exeter. Though our meet ups are rare, I always look  
40 forward to our group holidays and hope they continue far into the future.

41 Lorenza Iacobuzio, you get a special mention. While we weren't especially close until  
42 recently, you've been my sage, partner in food, and exceptional friend when I've needed it  
43 the most.

44 Finally, and most importantly, my family deserve my thanks. You have been there for me  
45 since the very beginning supporting me through school, undergrad, PhD, and every other  
46 endeavour. To my grandparents, uncles, aunties, and cousins, my siblings Joe, Lydia, Sitara,  
47 and Arjen, my stepmum Nadia, and my cat Pixie, I am sincerely grateful to have you in my  
48 lives. But above all else, to my mum Meeta and dad Kiron, I could not have done any of this  
49 without you and as such, you have my deepest and most heartfelt love and gratitude.

Draft: 13th April 2020

## AUTHOR'S DECLARATION

51 I declare that the work in this dissertation was carried out in accordance with  
52 the requirements of the University's *Regulations and Code of Practice for Re-*  
53 *search Degree Programmes* and that it has not been submitted for any other  
54 academic award. Except where indicated by specific reference in the text, the  
55 work is the candidate's own work. Work done in collaboration with, or with  
56 the assistance of, others, is indicated as such. Any views expressed in the disser-  
57 tation are those of the author.

58 SIGNED: ..... DATE: .....

Draft: 13th April 2020

## TABLE OF CONTENTS

	<b>Page</b>
<b>60 List of Figures</b>	<b>ix</b>
<b>61 List of Tables</b>	<b>xi</b>
<b>62 1 Introduction</b>	<b>1</b>
63   1.1 Evidence for dark matter . . . . .	1
64    1.1.1 Alternative theories to dark matter . . . . .	3
65   1.2 Overview of dark matter searches . . . . .	4
66    1.2.1 Dark matter searches at the LHC . . . . .	4
<b>67 2 Theory</b>	<b>9</b>
68   2.1 The standard model of particle physics . . . . .	9
69    2.1.1 Limitations of the standard model . . . . .	10
70   2.2 Theoretical motivations for, and descriptions of, dark matter . . . . .	11
71   2.3 Important observables and quantities in collider physics . . . . .	12
72    2.3.1 The electron volt . . . . .	13
73    2.3.2 Transverse momentum ( $p_T$ ) . . . . .	13
74    2.3.3 $H_T$ . . . . .	14
75    2.3.4 Missing transverse momentum ( $p_T^{\text{miss}}$ ) . . . . .	14
76   2.4 Measuring the branching ratio of invisibly decaying Higgs bosons . . . . .	15
77   2.5 Searches for semi-visible jets . . . . .	16
78    2.5.1 Kinematics and free parameters of the model . . . . .	17
<b>79 3 The LHC and the CMS experiment</b>	<b>21</b>
80   3.1 CERN . . . . .	21
81   3.2 The Large Hadron Collider . . . . .	23
82    3.2.1 A proton's journey . . . . .	23

---

## TABLE OF CONTENTS

83	3.2.2 Luminosity . . . . .	24
84	3.2.3 Pileup . . . . .	26
85	3.2.4 Evolution of the LHC . . . . .	27
86	3.3 The CMS experiment . . . . .	29
87	3.3.1 The CMS detector . . . . .	30
88	3.3.2 Data acquisition and triggering . . . . .	35
89	3.3.3 Simulating CMS data . . . . .	38
90	3.3.4 Jet energy corrections in the Level-1 Trigger . . . . .	39
91	<b>4 Combined search for invisibly decaying Higgs bosons in hadronic channels</b>	43
92	4.1 Analysis overview . . . . .	44
93	4.1.1 Hadronic production modes of the Higgs boson . . . . .	44
94	4.2 Categorisation of the non-VBF production modes . . . . .	44
95	4.3 Data and simulation . . . . .	44
96	4.3.1 Weights and corrections for simulated processes . . . . .	44
97	4.4 Triggers . . . . .	48
98	4.5 Background estimation . . . . .	48
99	4.5.1 Control regions . . . . .	48
100	4.5.2 Sidebands to the signal region . . . . .	48
101	4.5.3 Background estimation methods . . . . .	48
102	<b>5 Search for dark matter through the production of semi-visible jets</b>	49
103	5.1 Analysis overview . . . . .	50
104	5.2 Data and simulation . . . . .	50
105	5.2.1 Generating signal samples in PYTHIA . . . . .	50
106	5.2.2 Generating signal samples in MADGRAPH . . . . .	50
107	5.2.3 Triggers . . . . .	50
108	5.3 Background estimation . . . . .	50
109	<b>6 Conclusions</b>	51
110	<b>A Appendix A</b>	53
111	<b>Bibliography</b>	55
112	<b>Glossary</b>	65
113	<b>Acronyms</b>	67

## LIST OF FIGURES

	<b>FIGURE</b>	<b>Page</b>
115 1.1 A visual representation of the three main types of dark matter detection: direct, 116 indirect, and production . . . . .	5	
117 1.2 The expected masses and interaction cross sections of some dark matter can- 118 didates. The LHC, with its centre of mass energy of 13 TeV, is best suited to 119 targeting WIMPs . . . . .	6	
120 2.1 A measure of the comoving number density of WIMP dark matter as a function 121 of time with projections for different particle masses . . . . .	12	
122 2.2 Example Feynman diagrams for the two main production modes of semi-visible 123 jets. A $Z'$ boson mediates the $s$ -channel process while a bi-fundamental $\Phi$ medi- 124 ates the $t$ -channel process . . . . .	17	
125 2.3 The constituents of a semi-visible jet as a function of its invisible fraction . . . .	18	
126 2.4 The typical direction of the missing transverse energy relative to the semi-visible 127 jets as a function of the invisible fraction $r_{\text{inv}}$ . . . . .	18	
128 3.1 A schematic of the CERN accelerator complex . . . . .	25	
129 3.2 The average number of pileup interactions per bunch crossing at CMS during 130 Run-2 of the LHC . . . . .	27	
131 3.3 The integrated luminosity of $pp$ collision data delivered to CMS during Run-2 132 of the LHC . . . . .	28	
133 3.4 A cutaway diagram of the CMS detector with all of the principal components 134 labelled. This detector configuration was used for the 2017–18 data taking years	31	
135 3.5 A quadrant of the CMS detector illustrating the main subsystems with their 136 radius $R$ , longitudinal distance $z$ , and pseudorapidity $\eta$ from the interaction point	32	
137 3.6 A transverse slice through the barrel section of the CMS detector with the main 138 subsystems and components visible . . . . .	36	

## LIST OF FIGURES

---

139	3.7	A summary of the CMS Level-1 Trigger data flow from the hits recorded by the 140 subsystems to the Global Trigger . . . . .	37
141	3.8	Examples of correction curves used to calibrate the jet energies in two $ \eta $ bins .	41
142	3.9	The energies of matched pairs of jets in the entire barrel and end cap, in the 143 pileup 40–50 range, before and after jet energy corrections have been applied .	42
144	3.10	The response curves in each $ \eta $ bin as a function of $p_T^{L1}$ , in the pileup 40–50 145 range, before and after jet energy corrections are applied . . . . .	42
146	4.1	The Feynman diagrams for the four main hadronic production modes of the 147 Higgs boson . . . . .	45

**LIST OF TABLES**

TABLE	Page
149    3.1    The integrated luminosity delivered by the LHC during Run-2 which were re-	
150                corded and certified by CMS . . . . .	28
151    3.2    Some of the important parameters defining the performance of the LHC at the	
152                end of Run-2, for the High-Luminosity LHC, and the design specification . . .	29

Draft: 13th April 2020

## INTRODUCTION

153

154

155 The universe, in all its vastness, structure, natural laws and chaos, is comprised of only  
156 three principal components: visible matter, the ingredients of stars, planets and life,  
157 is the only one we interact with on a regular basis; dark energy, a force or manifest-  
158 ation of something even more mysterious, responsible for the accelerating expansion of the  
159 universe, is almost entirely unknown; and dark matter, a substance invisible in all sense of  
160 the word, that binds galaxies together and influences large scale structure in the cosmos, is  
161 the focus of this thesis.

## 162 1.1 Evidence for dark matter

163 The earliest evidence for a large, non-luminous component of the galaxy stretches back to  
164 the 1920s when Jacobus Kapteyn attempted to explain the motion of stars in the Milky  
165 Way [77]. Since then, a wealth of independent astrophysical observations have reinforced  
166 the existence of this aggregation not just in our own, but in countless other galaxies and  
167 cosmological bodies. The Coma Cluster is a famous example: 90 % of its mass is thought  
168 to arise from dark matter, confirmed by its large mass-to-light ratio of  $400 M_{\odot}/L_{\odot}$  [106].  
169 Further evidence is that the rotation curves of most galaxies are roughly flat [90], contrary  
170 to the expected Keplerian relationship ( $v_r \propto r^{-1/2}$ ) expected from solely visible matter.  
171 On a galactic scale, dark matter is sprinkled in a mostly spherical halo that spans beyond the  
172 observable disc. The inclusive dark matter mass increases linearly [55] to compensate for the  
173 decline expressed by visible matter [31, 61]. Gravitational lensing is another observational

174 tool subject to influence from dark matter. Images of galaxies and other objects captured by  
175 this method appear distorted from a large gravitational field between the source and observer  
176 warping its local spacetime [74]. Arcs, ellipses and Einstein rings of smeared galaxies are  
177 often seen when dark matter is present.

178 While there are no widely-accepted estimations, it is believed that 85–95 % of the Milky  
179 Way is comprised of dark matter [22, 23, 75]. Though these approximations include non-  
180 visible identifiable matter such as dim stars, black holes and neutron stars, the term “dark  
181 matter” typically reserved for the non-luminous, *non-baryonic* segment that pervades the  
182 cosmos. From the latest results of the Planck mission, the energy density of the observable  
183 universe is composed of 26.5 % dark matter [8]. This result follows the Lambda cold dark  
184 matter ( $\Lambda$ CDM) model to describe the constituents and evolution of the universe, which  
185 is often referred to as the cosmological analog of the standard model of particle physics  
186 (SM). From the calculations, postulations, and observations presented above, the following  
187 properties of dark matter can be deduced:

- 188 – It is electrically neutral as it does not interact with electromagnetic radiation. Hence,  
189 the adjective “dark” in dark matter.
- 190 – It is non-relativistic, or *cold*. Its velocity within galaxies is similar to the inhabiting  
191 stars [28, 72], since the combination of visible and dark matter drives the measured  
192 rotation curves. One small cayeat is that galactic dark matter *must* be cold since a  
193 velocity above the gravitational escape velocity of the galaxy would eject high speed  
194 particles.
- 195 – It is stable, at least on the timescale of the current age of the universe. Dark matter  
196 production is postulated to have occurred only in the early universe via a thermal  
197 freeze-out mechanism (see Chpt. 2.2). Hence, the remaining fraction has been present  
198 for a considerable time. Since most galaxies are dominated by dark matter and the  
199 gravitational influence from only the visible matter is too small to maintain itself, they  
200 could not have developed without it. This supports the idea of “bottom-up” structure  
201 formation in the universe; smaller galaxies form around gravitational potential wells  
202 provided by coalescing dark matter, then merge to form larger structures [105].
- 203 – Its interaction with matter and itself is very weak, or even non-existent. The Bullet  
204 Cluster—an astronomical object consisting of two colliding galaxy clusters—is the best  
205 example of this inference. From measurements of, predominantly, x-ray emission and  
206 gravitational lensing, it was found that while there is substantial dark matter present,  
207 interaction with itself and the visible matter surrounding it was minimal at most [39].

208 A kinematic explanation for the spherical distribution and low velocity of dark matter  
209 in galaxies can be explained by its collisionless nature. During the formation of a galaxy  
210 or stellar system, visible matter frequently collides, dissipating angular momentum and  
211 collapsing into a disc.

### 212 1.1.1 Alternative theories to dark matter

213 Though little is intrinsically known about dark matter since all evidence stems from its grav-  
214 itational influence, there are alternative theories that may explain the observations presented  
215 above. However, the scientific community can exclude many of these. Mismeasurements of  
216 the amount of baryonic matter such as neutrinos, neutrons, and interstellar gas are among  
217 the simpler propositions.

218 The neutrino flux from stars [REF] and the cosmic neutrino background [104] are pre-  
219 cise and well-tested. Even considering the upper limits on neutrino masses [86], they cannot  
220 make a significant contribution to the dark matter content in the universe. This is even dis-  
221 counting their highly relativistic nature, where myriad experimental evidence suggests dark  
222 matter is cold.

223 One can also use the Cosmic Microwave Background to calculate the average photon and  
224 neutrino densities, and Big Bang Nucleosynthesis calculations to determine the baryonic  
225 matter density (see Ref. 59 for results with the latest Planck mission data). These can be  
226 compared to other measurements, e.g., mass-to-light ratios averaged across the universe, to  
227 reveal a discrepancy [50].

228 Neutrons cannot contribute to dark matter because isolated neutrons are unstable, de-  
229 caying in a matter of minutes [88]. Transforming into charged protons and electrons, they  
230 interact strongly with light and therefore contribute to the luminous matter content.

231 Modified Newtonian dynamics (MOND) is a hypothesis that aims to explain phenom-  
232 ena typically associated with dark matter instead by modifications to Newton's laws of mo-  
233 tion. There exist many theories and interpretations derived from this principle, though any  
234 one strand that tries to explain an observation usually fails to satisfy other phenomena or  
235 apply to length scales that general relativity may predict well. For example, observations of  
236 the Bullet Cluster [39] have discredited many popular MOND models.

## 237 1.2 Overview of dark matter searches

238 While observational evidence has so far lain with astrophysics, a theoretical description and  
239 discovery of dark matter may fall into the realm of particle physics with the numerous, novel  
240 experimental searches underway. The detection of dark matter can be classified into three  
241 distinct methods with unique signatures (paired with a visual summary in Fig. 1.1):

- 242 – **Direct:** dark matter may interact with visible matter on small scales, scattering SM  
243 particles [92]. The recoil these SM particles experience could be detected by highly-  
244 sensitive, low background experiments such as LUX-ZEPLIN (LZ) [10] that specialises  
245 in the search for WIMP dark matter at a large range of masses.
- 246 – **Indirect:** if dark matter interacts with itself, it may annihilate to produce showers of  
247 high energy photons or pions. Background estimation is difficult since the signatures  
248 can be highly model-dependent. The particles may be of a continuum—from hadronisation  
249 and radiation of the decay products—or contain features, such as internal radiation  
250 from the propagator in the interaction or from loop-level processes [49]. Large ranges  
251 of the annihilation cross section and dark matter mass can be probed with telescopes  
252 already searching for these characteristic events.
- 253 – **Production:** dark matter may have been abundantly produced in the hot, early uni-  
254 verse. High energy particle accelerators such as the LHC can reproduce these condi-  
255 tions, with the WIMP miracle (see Chpt. 2.2) reinforcing the idea that dark matter may  
256 exist in these accessible mass ranges. Many beyond the standard model (BSM) theories  
257 accommodate dark matter candidates with a diverse spectrum of final states that can  
258 be investigated by analysing LHC data.

### 259 1.2.1 Dark matter searches at the LHC

260 Since detection at the CMS experiment from the production mechanism is the focus of this  
261 thesis, it is important to establish the current state of dark matter searches at the Large Had-  
262 ron Collider (LHC); the world’s most powerful particle accelerator that provides the infra-  
263 structure for CMS to collect data. Both machines are described in detail in Chpt. 3, and as  
264 such only a summary will be provided here. The LHC principally collides protons at centre  
265 of mass energies up to  $\sqrt{s} = 13$  TeV. These exceptionally high energies allow the conditions  
266 in the very early universe to be simulated in which heavy, unstable particles were produced  
267 plentifully. As a result, many theories can be investigated that predict heavy particles that do  
268 not exist in the universe today. Some of these, such as supersymmetry (SUSY) [85], sterile

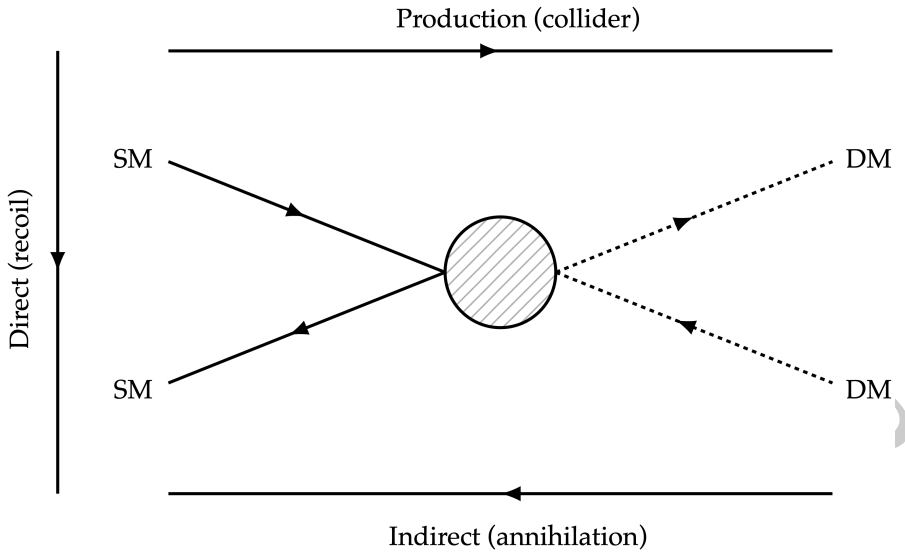


Figure 1.1: A visual representation of the three main types of dark matter detection: direct (dark matter recoiling from standard model particles); indirect (annihilation of dark matter); and production (dark matter created in high energy physics collisions).

269 neutrinos [54], and Kaluza-Klein states [67] contain dark matter candidates that can be spe-  
 270 cifically searched for, or indirectly inferred if a theory is experimentally proven. Despite the  
 271 success of the standard model in explaining much of the natural world, it does not substanti-  
 272 ate the existence of dark matter. BSM theories can therefore gain traction. Fig. 1.2 illustrates  
 273 the masses and interaction cross sections of many dark matter candidates. Weakly Interact-  
 274 ing Massive Particles (WIMPs) (highlighted by the purple rectangle) are the the subject of  
 275 many searches at the LHC since the expected mass ranges and cross sections are accessible  
 276 there.

277 Two avenues are usually considered when attempting to discover dark matter: explicit  
 278 searches for the signatures of dark matter production, and anomalies in precision measure-  
 279 ments. The former is quite common, with many theories and models tested at the LHC's  
 280 general purpose detectors, ATLAS and CMS. Searches at CMS have been performed for  
 281 promptly-decaying and “long-lived” supersymmetry in hadronic final states (in which I made  
 282 contributions) [79, 95]. Searches for specific supersymmetric particles in a variety of decay  
 283 modes have been conducted by both experiments [34]. In many of these cases, the lightest  
 284 supersymmetric particle (LSP) is considered to be a dark matter candidate.  $R$ -parity con-  
 285 servation is predicted (or even enforced) in many SUSY models [85], which prevents the  
 286 decay of LSP and any lighter, standard model particles that have been observed to be stable.  
 287 While supersymmetry is the most popular BSM theory, due in part to its numerous inter-

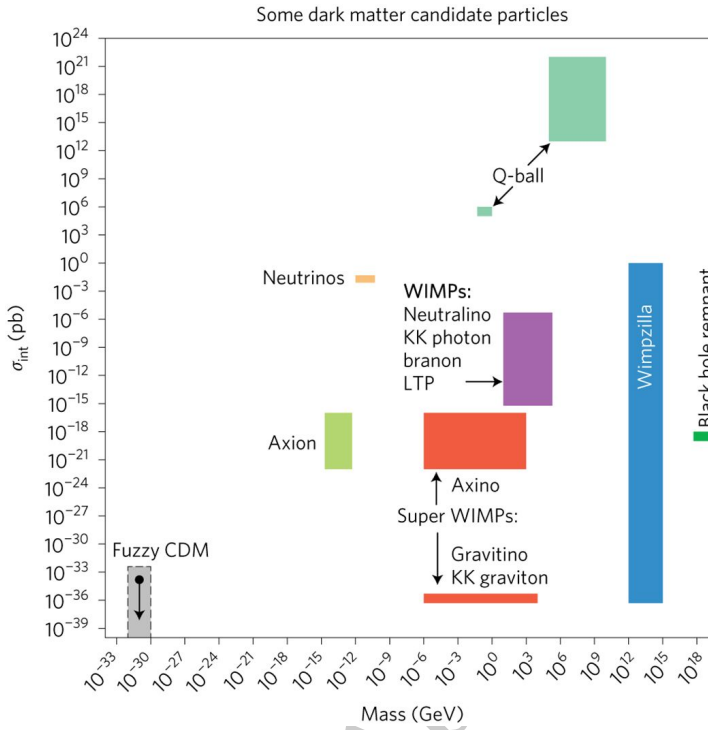


Figure 1.2: The expected masses and interaction cross sections of some dark matter candidates. The LHC, with its centre of mass energy of 13 TeV, is best suited to targeting WIMPs. Figure acquired from Ref. 49.

288 pretations and approaches for discovery, many others have also been explored at the LHC.  
 289 From microscopic black holes [81], to [OTHERS], there are extensive propositions that  
 290 have the potential to uproot the standard model. The analyses above are usually character-  
 291 ised by large “missing” transverse momentum (explained further in Chpt. 2.3.4), a quantity  
 292 that represents the momenta of particles invisible to the detector, such as dark matter. In  
 293 Chpt. 5, I discuss in detail a search for dark matter that utilises this variable.

294 Precision measurements of standard model parameters is the other method often consul-  
 295 ted in the hopes of attributing anomalies to new physics. For example, attempts to explain  
 296 anomalies in the  $b \rightarrow s$  transition include dark matter candidates [35, 103]. In Chpt. 4, I  
 297 investigate how the measurement of the Higgs boson to invisible state branching ratio can  
 298 accommodate dark matter.<sup>1</sup>

299 There is significant motivation to study dark matter from a wider, as well as a more  
 300 personal, viewpoint. It is important to understand how the universe operates, and dark  
 301 matter opens up the potential for new physics that improves our understanding of nature.  
 302 My personal interests include the blend of particle physics and astrophysics, the opportunity

<sup>1</sup>Maybe add another example of anomalies in precision measurements

## 1.2. OVERVIEW OF DARK MATTER SEARCHES

---

303 to discover, and add to humanity’s collective wisdom. With  $137 \text{ fb}^{-1}$  at  $\sqrt{s} = 13 \text{ TeV}$  from  
304 CMS during Run-2 of the LHC, there is great potential to constrain some of the properties  
305 of dark matter. This thesis showcases the motivation for, and results of, searches for invisibly  
306 decaying Higgs bosons and semi-visible jets with the full Run-2 dataset collected by the CMS  
307 experiment.<sup>2</sup>

Draft: 13th April 2020

---

<sup>2</sup>Add another figure or two somewhere to help separate the text? Maybe an astronomical image of the Bullet Cluster/dark matter distribution in a cosmological object, or a gravitational lensing ring from dark matter

Draft: 13th April 2020

308

309

## THEORY

310 This thesis is comprised of experimental searches for dark matter and new physics. The  
311 experimental chapters Chpt. 4 and Chpt. 5 delve deeply into the analyses. Before  
312 which, the theoretical and phenomenological motivations must be understood to  
313 corroborate the need for them at the Large Hadron Collider. In this chapter, a brief recap  
314 of the standard model will be presented along with its shortcomings, foremost the lack  
315 of a dark matter candidate. Theoretical descriptions of dark matter that best fit the relic  
316 density and astrophysical observations will then be discussed. Specific interpretations in the  
317 forms of semi-visible jets and invisibly decaying Higgs bosons are examined that provide the  
318 background for the respective analysis chapters.

319 **2.1 The standard model of particle physics**

- 320 – Give an overview of the fundamental forces and particles in a QFT/group theory  
321 context.
  - 322 • May have to mention chirality and helicity, briefly, in relation to “handedness”  
323 of particles.
  - 324 – Discuss the standard model in some amount of detail, emphasizing certain aspects as  
325 they relate to the Higgs field & boson.
    - 326 • Mention resonances and widths. Each decay mode of a particle contributes a par-  
327 tial width (which determines its branching ratio:  $\mathcal{B}$  = partial width/total width).

- 328       • Talk in some detail about the Higgs mechanism as that will inform the Higgs to  
329            invisible section. Mention Yukawa coupling to fermions, and that it's dependent  
330            on the squared mass of the decay products. Lends credence to suppression of  
331            direct decay to neutrinos (assuming they even couple to Higgs).

332 **2.1.1 Limitations of the standard model**

333 Despite the standard model providing precise predictions of three of the four fundamental  
334 forces and the particles that they interact with, there are many experimental observations  
335 that it cannot currently explain. Neutrino masses, dark matter, dark energy, and gravity all  
336 escape its description.

337       The Hierarchy Problem is one of the more serious issues facing the standard model. It  
338       may be explained in different manners that emphasize certain aspects. But inherently, it is  
339       a question of the disparity between energy scales of the fundamental forces—particularly  
340       relating to the weak force and gravity. The masses of the intermediate vector, and Higgs,  
341       bosons of  $\mathcal{O}(100 \text{ GeV}/c^2)$  are much smaller than the Planck mass of  $\mathcal{O}(10^{19} \text{ GeV}/c^2)$ .  
342       The mass term for the Higgs boson is  $m^2 H^\dagger H$  in the SM. Invariance under a gauge or global  
343       symmetry in the Higgs field  $H$  leads to the mass being open to radiative corrections up to  
344       the Planck scale.<sup>1</sup> It appears that, in nature, these very large terms cancel to give the familiar  
345        $m_H = 125 \text{ GeV}/c^2$  [5, 37]. It is deemed unnatural to expect cancellations to such a degree,  
346       i.e., one part in  $10^{17}$ . This “fine-tuning” of parameters in the standard model is something  
347       that unified or natural theories desperately try to avoid.

348       Some BSM theories like supersymmetry provide well-motivated cancellations by intro-  
349       ducing supersymmetric particles. In certain scenarios, some of these particles should exist  
350       at the TeV scale. In the SM, the largest correction to the Higgs mass derives from the top  
351       quark, since its Yukawa coupling to the Higgs is the strongest. At one-loop order, new phys-  
352       ics at  $\mathcal{O}(\text{TeV})$  scale is required, with new particles coupling to the Higgs field to prevent  
353       these corrections from being unreasonably large [58]. Arguments such as this give credence  
354       to new physics being discoverable at particle accelerators such as the Large Hadron Collider.

---

<sup>1</sup>Justify this more?

355 **2.2 Theoretical motivations for, and descriptions of, dark  
356 matter**

357 Dark matter may have been forged in the universe via one of many possible mechanisms.  
 358 The most popular is described as a *thermal freeze-out* process. In the hot, early universe when  
 359 the thermal background allowed spontaneous pair production of particle dark matter, it was  
 360 generated in abundance. During this period, the particles may also have frequently annihilated  
 361 seeing that the cosmos was still small. Inevitably, the universe expanded and cooled; the  
 362 temperature became too low to allow significant production [20]. Matter was further  
 363 separated and the dark matter annihilation rate decreased, leaving a behind the “thermal  
 364 relic” that is observed today. These remaining particles were attracted via gravity, forming  
 365 filaments throughout the universe. The potential wells they induced allowed the progenitors  
 366 of galaxies to form within.

367 Full derivations of the thermal freeze-out of dark matter<sup>2</sup> can be found in literature  
 368 [25, 63], with the WIMP Miracle as a consequence: with relatively few assumptions, the  
 369 correct dark matter relic abundance can be recovered by requiring a WIMP mass of  $\mathcal{O}(\text{GeV} -$   
 370  $\text{TeV})$ , dependent on the annihilation cross section. This is a range accessible at contemporary  
 371 colliders such as the LHC, and perhaps coincidentally, around the electroweak energy scale.  
 372 It is common for figures that depict the WIMP dark matter density over time to plot the  
 373 yield  $n_\chi/s$  as a function of the dimensionless parameter  $x = m_\chi/T$ . In the former variable,  $n_\chi$   
 374 is the number density and  $s$  is the entropy density. In the latter,  $m_\chi$  is the dark matter mass  
 375 and  $T$  is the average temperature of the universe, which serves as a measure of its age due to  
 376 the temperature decreasing over time. An example is given in Fig. 2.1.

377 The time of the dark matter freeze out epoch is somewhat insensitive to the mass and an-  
 378 nihilation cross section. Approximate solutions to the Boltzmann equation for time-dependent  
 379  $n_\chi$ —where dark matter is modelled as a weakly-interacting, diffuse gas of particles—suggest  
 380  $x_f \sim 20$  [25, 84]. Stronger dark matter interaction leads to decoupling at a later time and  
 381 a lower number density. The approximate value of  $x_f$  is significant in that it supports the  
 382 electroweak-scale mass of WIMPs.

383 Another popular mechanism, targeting low-mass dark matter, is the *freeze-in* process [65,  
 384 82]. In this postulate, dark matter is not produced thermally in the early universe. Instead,  
 385 it emerges through interactions between SM particles such as collisions, or decays of those  
 386 heavier than dark matter. The comoving density increases with time until it plateaus from of

---

<sup>2</sup>Is it worth going through the derivation, maybe as an appendix? It might be superfluous considering it's already described in literature.

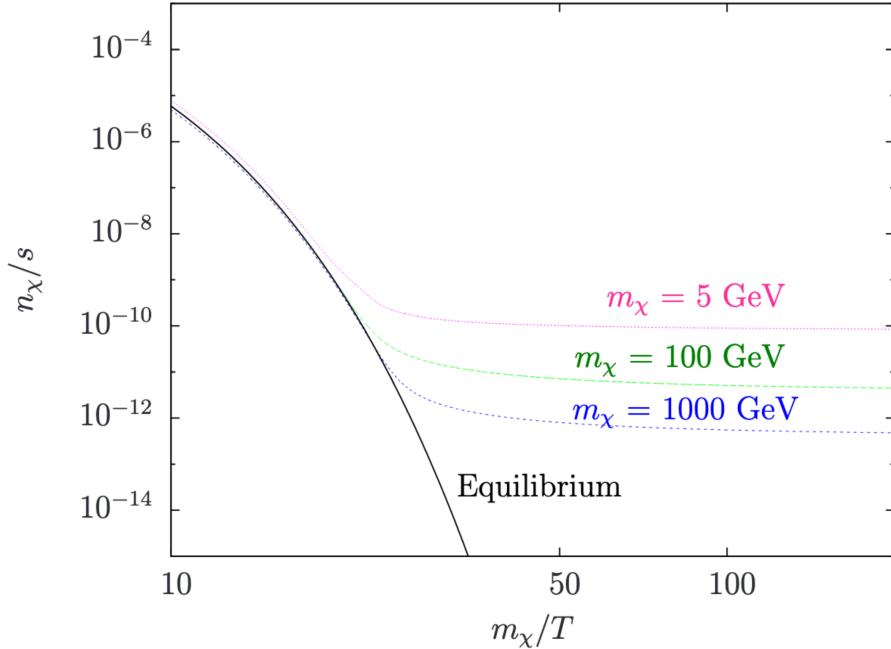


Figure 2.1: A measure of the comoving number density of WIMP dark matter as a function of time with projections for different particle masses. A higher mass must be balanced by a larger annihilation cross section to achieve the correct relic density, to which it tends asymptotically from the point of decoupling. The black curve represents the scenario in which dark matter remains in equilibrium with the standard model. Figure taken from Ref. 66.

387 the cooling of the universe, where SM particles are generally stable enough and too low en-  
 388 ergy to produce dark matter in any meaningful quantity. The relic abundance can therefore  
 389 reclaimed from a combination of the initial thermal distributions, the dark matter mass, and  
 390 the interaction strength, similar to the freeze-out process. In order to obey cosmological ob-  
 391 servations, particularly the fact that it is cold, the masses expected for freeze-in dark matter  
 392 particles are of  $\mathcal{O}(\text{keV})$  or heavier.<sup>3</sup>

### 393 2.3 Important observables and quantities in collider 394 physics

395 The following section discusses some ubiquitous variables and units in high energy phys-  
 396 ics, particularly in the context of colliders. Accordingly, it is [useful] to consolidate their

<sup>3</sup>Could also briefly describe other interpretations of dark matter relic abundance? For all of these cases, not sure how much detail I should go in to, in terms of quantitative derivations.

397 definitions here.<sup>4</sup>

398 **2.3.1 The electron volt**

In highly relativistic systems, such as beams of particles in accelerators, the ability to simply equate mass, energy, and momentum is desirable. In the LHC, when protons are accelerated to an enormous Lorentz boost factor, their invariant mass  $m_0$  contributes little to their total energy  $E$ . With Einstein's energy-momentum relation from the special theory of relativity, one can express the energy as functions of intrinsic mass and relativistic momentum:

$$(2.1) \quad E = \sqrt{(pc)^2 + (m_0 c^2)^2}$$

399 where  $p$  is the magnitude of the momentum and  $c$  is the speed of light. For highly relativistic  
400 objects,  $pc \gg m_0 c^2$  and so  $E \approx pc$ . At rest,  $E = m_0 c^2$ . The electron volt (eV) unit is  
401 common in high energy physics. Its value is the energy supplied to (or removed from) an  
402 electron accelerated through a potential difference of 1 V:  $1.6 \times 10^{-19}$  J. The momentum  
403 gained is then  $1 \text{ eV}/c$  and relativistic mass  $1 \text{ eV}/c^2$ . The factors of  $c$  and  $c^2$  are often dropped  
404 in less formal contexts, or when using natural units (where  $c = 1$ ).

405 An electron volt is a minute quantity of energy, so when discussing properties of high  
406 energy particles and accelerators, a long string of digits may be required to express them. SI  
407 prefixes mitigate this problem and provide an intuitive sense of scale to scientists. The most  
408 frequently used in the context of LHC physics are *mega* (M,  $10^6$ ), *giga* (G,  $10^9$ ), and *tera*  
409 (T,  $10^{12}$ ). For example, the mass of a proton is  $0.93 \text{ GeV}/c^2$  and the present centre of mass  
410 energy of the LHC is  $13 \text{ TeV}$ , which are much more natural and understandable numbers  
411 than  $1.78 \times 10^{-27} \text{ kg}$  or  $1.6 \times 10^{-7} \text{ J}$ , respectively.

412 **2.3.2 Transverse momentum ( $p_T$ )**

413 In the LHC (or any other collider), the longitudinal momentum of the initial state particles  
414 is typically unknown. However, the momentum transverse to the beam is zero before the  
415 collision, and must be zero afterward due to momentum conservation. This is why the  
416 transverse momentum of a particle or physics object ( $\vec{p}_T$  for the vector quantity,  $p_T$  for its  
417 magnitude) is a useful variable in an analysis.<sup>5</sup>

---

<sup>4</sup>The theory chapter is probably not the right place to put this section. Maybe a separate section or appendix would be better.

<sup>5</sup>Do I need a more formal/mathematical definition? Could just reference geometry section in detector chapter.

418 **2.3.3  $H_T$**

The outcome of a collision in the LHC is referred to as an *event*. The hadronic constituents in an event often shower due to colour confinement, producing collimated sprays of hadrons called *jets*. For analyses focused on hadronic objects—such as branches of supersymmetry where a large jet multiplicity is expected—it is practical to define the total amount of hadronic activity in an event. The scalar sum of the transverse momentum of the jets is symbolised as  $H_T$ :

$$(2.2) \quad H_T \equiv \sum_{\text{jets}} p_T$$

419 Typically, a lower limit on the  $p_T$  is used when calculating the  $H_T$ , so jets below this threshold  
 420 do not factor into the sum. This is to avoid low momentum jets attributed to pileup events  
 421 (see Chpt. 3.2.3), and those from the primary vertex that can often be mismeasured.

422 **2.3.4 Missing transverse momentum ( $\vec{p}_T^{\text{miss}}$ )**

The missing transverse momentum  $\vec{p}_T^{\text{miss}}$  is defined as the negative vector sum of the  $\vec{p}_T$  of all identified particles in an event. It is a term often used interchangeably with missing transverse energy (MET,  $\vec{E}_T^{\text{miss}}$ ). Undetected particles from neutrinos or dark matter, or mismeasured kinematic properties of identified particles, will introduce an imbalance in the vector sum of the  $\vec{p}_T$ . Hence, the  $\vec{p}_T^{\text{miss}}$  will be non-zero.<sup>6</sup> Formally,

$$(2.3) \quad \begin{aligned} \vec{p}_T^{\text{miss}} &\equiv - \sum_i^{N_{\text{particles}}} \vec{p}_{T,i} \\ p_T^{\text{miss}} &\equiv |\vec{p}_T^{\text{miss}}| \end{aligned}$$

The hadronic-only counterpart to this variable,  $\vec{H}_T^{\text{miss}}$ , is the negative vector sum of the jet transverse momenta in an event:

$$(2.4) \quad \begin{aligned} \vec{H}_T^{\text{miss}} &\equiv - \sum_j^{N_{\text{jets}}} \vec{p}_{T,j} \\ H_T^{\text{miss}} &\equiv |\vec{H}_T^{\text{miss}}| \end{aligned}$$

423 As with  $H_T$ , the  $H_T^{\text{miss}}$  is often calculated with a lower limit on the jet  $p_T$ .

---

<sup>6</sup>A depiction of the MET (e.g., SM particles recoiling off dark matter) might be useful for the reader.

424 **2.4 Measuring the branching ratio of invisibly decaying**  
 425 **Higgs bosons**

426 The Higgs boson has caught the attention of the high energy physics community, and even  
 427 the public eye, like no other particle in recent memory. Its discovery in the  $H \rightarrow \gamma\gamma$  channel  
 428 in 2012—*independently by both CMS [37] and ATLAS [5]*—realised one of the paramount  
 429 goals of the LHC’s construction. The particle itself is not necessarily exciting. Rather, it  
 430 confirms the existence of the Higgs *field* that pervades the universe and gives mass to the  
 431 elementary particles via the exchange of its eponymous boson [56, 64, 73]. Its discovery,  
 432 one might think, was the end of the discussion of the Higgs boson. However, it was only  
 433 the beginning.

434 Many observations of the Higgs, such as its predominant decay mode  $H \rightarrow b\bar{b}$ , were  
 435 not seen until recently by CMS [93] or ATLAS [4]. Constraints on its other properties have  
 436 also been placed, such as its resonance width and branching ratios  $\mathcal{B}$  to several final states.  
 437 Fully understanding the Higgs boson is important to understanding the Higgs field and the  
 438 wider standard model. Precision measurements in tension with SM predictions can also be  
 439 a window to new physics. Measuring the  $H \rightarrow \text{inv.}$  branching ratio aims to do just that.

440 The only SM process in which Higgs boson can decay invisibly<sup>7</sup> is  $H \rightarrow ZZ \rightarrow 4\nu$   
 441 with a branching ratio of  $\mathcal{O}(0.1\%)$  [70]. The leading observed experimental upper limits  
 442 on this measurement are 19 % from CMS [97] and 26 % from ATLAS [3], far higher than  
 443 the predicted value. If undiscovered invisible particles, perhaps dark matter, couple to the  
 444 Higgs field the branching ratio will be enhanced.<sup>8</sup> Experimental evidence shows the coupling  
 445 strength to proportionally follow the mass of the particle, as verified in ATLAS and CMS’  
 446 latest measurements [100]. A considerably large enhancement may allow for this process to  
 447 be observed at the LHC. At the very least, a more accurate constraint on the branching ratio  
 448 is able to exclude some models of dark matter, such as those described in Refs. 53, 76.

449 There is no reason to assume dark matter does *not* interact with the Higgs field, since it  
 450 bestows mass to all known elementary particles (a small caveat, perhaps, being neutrinos).<sup>9</sup>  
 451 Higgs “portal” models have been theorised that connect the visible sector of the standard  
 452 model to a dark sector where particle dark matter resides [15, 18]. Certain models also

---

<sup>7</sup>A direct decay to neutrinos is possible if they acquire their mass from the Higgs field. But as the coupling is of a Yukawa form and the upper limit on the SM neutrino masses is very small, the branching ratio is expected to be heavily suppressed.

<sup>8</sup>Do I need to give a more mathematical motivation for the BR being enhanced/what kind of values the BR is expected to be from various DM models?

<sup>9</sup>Do I need to give some mathematical motivation as to *why* dark matter would couple to the Higgs? Or is the fact that it has mass enough justification?

453 predict a detectable presence at the LHC from a sufficient production rate [30], perhaps  
454 even with data obtained during Run-2 [7].

455 **2.5 Searches for semi-visible jets**

456 Many searches for dark matter presume it is a WIMP-like particle because of the considera-  
457 tions discussed in Chpt. 2.2. In the LHC, the signatures of WIMPs would be driven by large  
458 missing transverse momentum recoiling from visible matter in the event. Monojet [80] and  
459 dijet [96] searches are able to exploit this, for example. However, no sign of WIMPs have  
460 been observed yet. Thankfully, a boundless supply of alternative theories exist, with pos-  
461 sible signatures equally as varied. Though the  $p_T^{\text{miss}}$  could still be one of the characteristics by  
462 which the dark matter can be inferred, a plethora of topologies and discriminating observ-  
463 ables are possible. The dynamics that govern dark matter may be confined to a *dark sector*  
464 or *hidden sector*, inhabited by new forces and particles.

465 A dark sector may be largely inaccessible, as in some Hidden Valley<sup>10</sup> scenarios [101],  
466 but communicate with the visible sector through a portal interaction. An example from SM  
467 particles could be the Higgs boson bridging the visible and hidden sectors, as mentioned in  
468 Chpt. 2.4. Many interesting and novel signatures can be probed by LHC experiments from  
469 models like these. Dark forces with energy scales in the tens of GeV and mediator masses  
470 up to several TeV may be accessible. If they are analogous with the standard model, the  
471 mechanisms can be explained for the dark matter presence and relic density arising from a  
472 baryon-like asymmetry.

473 Proposed in Refs. 40, 41, a strongly-coupled dark sector in a Hidden Valley is imagined  
474 with interactions analogous to QCD.<sup>11</sup> The portals allowing the dark and visible sectors  
475 to communicate can be decomposed into a leptophobic  $Z'$  (*s*-channel) and bi-fundamental  
476  $\Phi$  (*t*-channel) mediator. In the *t*-channel case,  $\Phi$  is a representation of both the visible and  
477 dark QCD gauge groups. Depictions of the processes above are given in Fig. 2.2. In the  
478 LHC, protons could collide at energies high enough to access the dark sector. From either  
479 the resonant production of a  $Z'$  or exchange of a  $\Phi$ , dark quarks  $\chi^{12}$  are produced. Below a  
480 dark confinement scale  $\Lambda_{\text{dark}}$ , hadronisation takes place to coalesce them into dark hadrons.

---

<sup>10</sup>A Hidden Valley is a schema where the standard model is extended by a non-abelian group. SM particles are uncharged under this group. The new, light particles from this extension are the opposite: charged under the new group and neutral under the SM gauge group. A heavy mediator carries both charges, acting as a portal between the standard model and Hidden Valley particles.

<sup>11</sup>Do I need to mention that this dark sector is  $SU(2)_{\text{dark}}$ , and write the lagrangian for how it couples to SM via dark weak force?

<sup>12</sup>Not to be confused with stable dark matter that is often denoted by the symbol  $\chi$ .

481 Depending on the species, some of these dark hadrons are stable (i.e., a source of dark mat-  
 482 ter), while others are unstable and decay back into visible sector particles, namely standard  
 483 model quarks. The final state is then a shower of two jets each interspersed with dark matter:  
 484 *semi-visible jets*.

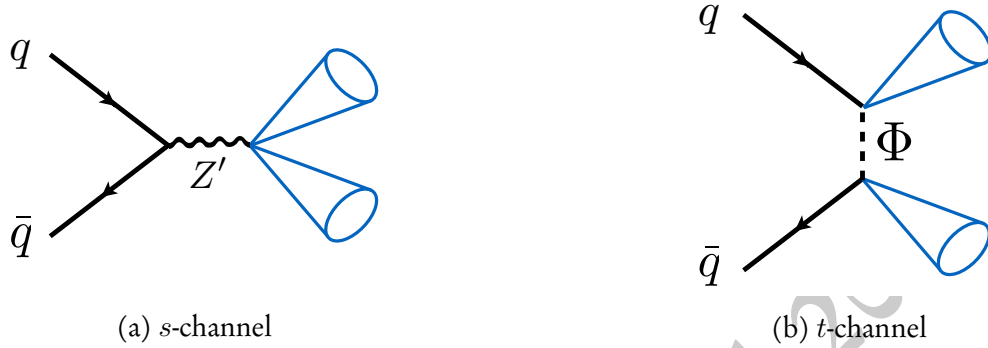


Figure 2.2: Example Feynman diagrams for the two main production modes of semi-visible jets. A  $Z'$  boson mediates the *s*-channel process while a bi-fundamental  $\Phi$  mediates the *t*-channel process. Figure from Ref. 41.

### 485 2.5.1 Kinematics and free parameters of the model

486 The kinematics of semi-visible jets are heavily influenced by the following free parameters  
 487 of the model: the mass of the mediator ( $m_{Z'}$  or  $m_\Phi$ ), the dark coupling strength ( $\alpha_{\text{dark}}$ ), the  
 488 dark quark mass ( $m_\chi$ ), and the invisible fraction ( $r_{\text{inv}}$ ).

489 –  $m_{Z'}/m_\Phi$ : Since the energies of the colliding protons have an upper limit, the conserva-  
 490 tion of energy (or momentum) imposes one for the on-shell production/exchange of  
 491 the mediator particle. In the *s*-channel process, production of the  $Z'$  is resonant. Con-  
 492sequently, its mass is possible to recover by calculating the dijet mass  $m_{\text{jj}}$  or transverse  
 493 mass  $M_T$ .

494 –  $\alpha_{\text{dark}}$ : In Ref. 41, this is defined as  $g_{\text{dark}}^2/4\pi$  (where  $g_{\text{dark}}$  is the coupling constant  
 495 between the dark quarks and mediator). Analogous to QCD, the dark coupling runs  
 as a function of the energy scale, influencing  $\Lambda_{\text{dark}}$ . At 1 TeV,

$$(2.5) \quad \Lambda_{\text{dark}} = 1000 \text{ [GeV]} \exp\left(\frac{-2\pi}{\alpha_{\text{dark}} b}\right)$$

496 where  $b = \frac{11}{3}N_c - \frac{2}{3}N_f$  is related to the number of dark colours and flavours, respec-  
 497 tively.

498 –  $m_\chi$ : This parameter does not directly affect much, but is related to the dark hadron mass  
 499 ( $2m_\chi$ ) and  $\Lambda_{\text{dark}}$ . The combination of the two properties affects the shower dynamics.

498 Note that while Ref. 41 describes some of these to be insensitive, a parameter scan  
 499 over these two variables are necessary in the search described in Chpt. 5.

500 –  $r_{\text{inv}}$ : This is defined as the fraction of produced invisible particles that remain stable, at  
 501 least over timescales where they interact with a detector. When generating simulated  
 502 samples,  $r_{\text{inv}}$  can be interpreted as the *probability* of a dark hadron remaining stable.  
 503 While this variable is not inherent within the model, it is one that can parametrise  
 504 many underlying components. As a result, visualisation of the shower and direction of  
 505  $\vec{p}_{\text{T}}^{\text{miss}}$  is much more intuitive, as demonstrated in Figs. 2.3 and 2.4, respectively. A large  
 506 value of  $r_{\text{inv}}$  would yield a similar final state to a WIMP search.

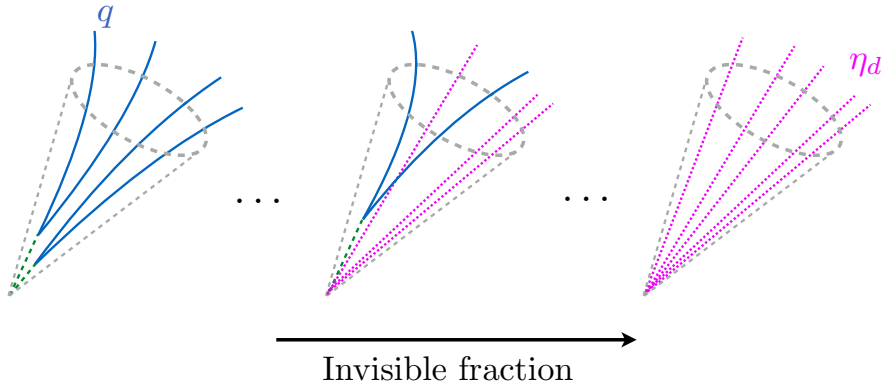


Figure 2.3: The constituents of a semi-visible jet as a function of its invisible fraction  $r_{\text{inv}}$ .  
 Figure taken from Ref. 41.

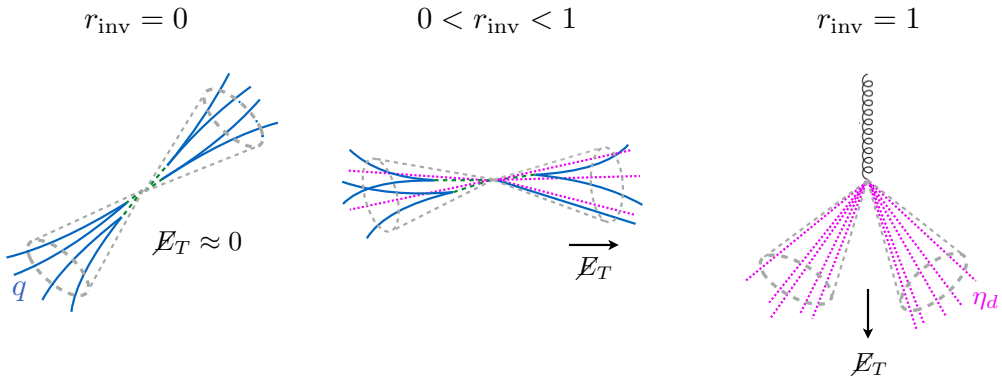


Figure 2.4: The typical direction of the missing transverse energy  $\cancel{E}_{\text{T}}$  (or  $p_{\text{T}}^{\text{miss}}$ ) relative to the semi-visible jets as a function of their invisible fraction  $r_{\text{inv}}$ . Figure from Ref. 41.

507 In the search for semi-visible jets in Chpt. 5, only the *s*-channel process has been analysed  
 508 with LHC data. Generator studies have been additionally performed for the *t*-channel inter-  
 509 action and the analysis is underway. In the *s*-channel search, mediator masses of up to several

510 TeV are accessible, and intermediate values of  $r_{\text{inv}}$  are most sensitive. Hence, the typical sig-  
511 nature is a dijet pair with each jet likely to contain a different invisible fraction, leading to  
512 the  $\bar{p}_T^{\text{miss}}$  aligned with one of the jets. WIMPs, on the other hand, completely recoil from the  
513 visible matter, and so jets may be more collimated with small separation. The  $p_T^{\text{miss}}$  is also  
514 larger and possibly more isolated. The phase space exploited by this model is often rejected  
515 by dark matter searches since the final state can be easily mimicked by mismeasured QCD.  
516 A sizeable background from this process would therefore be present. However, jet substruc-  
517 ture techniques and machine learning algorithms have developed rapidly in the recent years,  
518 and it is possible to disentangle signal and background with some certainty.

519 One interesting aspect of the model is the potential for signatures with displaced vertices,  
520 so called “long-lived” particles or “emerging jets” on account of the decay to visible states  
521 occurs a sufficient distance from the primary vertex. Some searches have already been per-  
522 formed for this final state from a different interpretation of a strongly-coupled dark force [98]  
523 to supersymmetry contexts [95]. These are not considered in Chpt. 5, so the dark hadrons  
524 are assumed to decay promptly. Long-lived interpretations have been noted as possible ex-  
525 tensions to the search, however.

Draft: 13th April 2020

526

527

## THE LHC AND THE CMS EXPERIMENT

528 This chapter concerns the experimental setup. CERN is the organisation that manages  
529 the machines discussed and is a pioneer in the high energy physics community. As  
530 such, it will be given a short overview. The Large Hadron Collider provides the CMS  
531 experiment with proton-proton collision data that is then stored, corrected, and then used  
532 by physicists for analysis. Ranging from standard model precision measurements, searches  
533 for new physics, the development of tools and algorithms to aid the previous two, these and  
534 much more are studied by the collaboration. CMS is described in detail, from its hardware  
535 and subdetectors to its data acquisition and trigger system. Special attention is given to the  
536 derivation of jet energy corrections (JEC) in the Level-1 Trigger (L1T) as I have been a part  
537 of that effort during my PhD.

### 538 3.1 CERN

539 CERN, the European Organisation for Nuclear Research (*Organisation Européenne pour la*  
540 *Recherche Nucléaire*), is the body responsible for large scale particle and high energy physics  
541 projects in Europe. It was founded in 1954 under the *Conseil Européen pour la Recherche Nucl*  
542 *éaire* (European Council for Nuclear Research), from where its acronym is derived. CERN's  
543 primary site is situated in the canton of Geneva and creeps over the Franco-Swiss border.  
544 Its main purpose today is to provide physical and technological infrastructure for particle  
545 and high energy physics experiments. From large scale accelerators to extensive computing  
546 farms, CERN has grown into the largest laboratory for particle physics in the world. The

547 organisation also provides a central community for the many researchers, engineers, and  
548 technicians to share ideas and collaborate effectively.

549 The organisation was founded by twelve European member states, the United Kingdom  
550 being one of them. It has since expanded to twenty three, encompassing most of western  
551 Europe and some of the continent’s east. Many more countries from across the globe are  
552 affiliated with CERN in some way, providing researchers, computing resources, and more.  
553 The member states and associated members contribute to CERN’s budget, to the tune of  
554 1.2 billion Swiss Francs for the year 2020 [60].

555 Many important inventions and discoveries can be attributed to CERN and its person-  
556 nel. Physics accomplishments include observations of weak neutral current interactions in  
557 1973 [68, 69], paving the way for the  $W$  [16, 21] and  $Z$  [17, 19] boson discoveries with the  
558 UA1 and UA2 experiments in 1983. The number of light neutrino generations at the Large  
559 Electron-Positron Collider (LEP) in 1989 [102], and direct CP violation with the NA48 ex-  
560 periment in 1999 [57], were also observed. Tim Berners-Lee and Robert Cailliau are credited  
561 with inventing the World Wide Web—the ubiquitous service for accessing the internet—in  
562 1989/90.

563 CERN is perhaps most widely known as the home of the Large Hadron Collider, the  
564 particle accelerator involved in the discovery of the Higgs boson [5, 37]. More details regard-  
565 ing the machine are discussed in Chpt. 3.2. But CERN is involved in many more undertak-  
566 ings. There are many fixed target experiments that use beams from the PS and SPS such as  
567 COMPASS, that studies hadronic structure, and NA62, investigating rare decays of kaons.  
568 Experiments like ALPHA and AEGIS use antiprotons from the Antiproton Decelerator to  
569 study antimatter in detail. The ISOLDE facility at CERN delivers beams of radioactive ions  
570 to perform many nuclear physics experiments.

571 Concern is given not just to contemporary science, but also to the physics of tomorrow.  
572 The experiments and accelerators are frequently upgraded, in particular the LHC improve-  
573 ments documented in Chpt. 3.2.4. Advanced accelerators are also being discussed, such as  
574 the Future Circular Collider (FCC). It would use the LHC as a booster, with the final ring  
575 having a 90–100 km circumference and up to 100 TeV centre of mass energy. Proposals for  
576 the injectants are electron-positron beams (FCC-ee,  $\sqrt{s} = 90\text{--}350 \text{ GeV}$ ) or proton-proton  
577 beams (FCC-hh,  $\sqrt{s} = 100 \text{ TeV}$ ). Each option boasts its own merits, and in an integrated  
578 scenario the former may be used as an intermediate step toward the latter.

## 579 3.2 The Large Hadron Collider

580 Deep underground beneath the Franco-Swiss border lies the Large Hadron Collider (LHC),  
 581 a synchrotron particle accelerator 27 km in circumference. As the largest machine in the  
 582 world, the LHC stands as a testament to the importance of fundamental science and the  
 583 dedication to which it is pursued. Predominantly a proton collider, lead and xenon ions  
 584 have also been injected for novel and unique studies. Four primary experiments are situated  
 585 at their own interaction points where the two beams of particles are brought into contact:  
 586 CMS (Compact Muon Solenoid), a general purpose detector with interests in precision meas-  
 587 urements, searches for new physics, and many other avenues; ATLAS (A Toroidal LHC Ap-  
 588 paratuS), a counterpart to CMS at its antipode on the LHC ring; LHCb, designed to study  
 589 the decay of  $B$  hadrons; and ALICE (A Large Ion Collider Experiment), primarily studying  
 590 heavy ion collisions and the quark-gluon plasma.

591 Four additional, smaller experiments are stationed in the LHC tunnel that are much  
 592 more specialised than those aforementioned: TOTEM (TOTal Elastic and diffractive cross  
 593 section Measurement) shares the CMS cavern with three subdetectors positioned near the  
 594 beam line, performing proton structure and interaction cross section studies; LHCf shares  
 595 the ATLAS cavity and is concerned with detecting neutral pions in the forward direction  
 596 to explain the origins of high energy cosmic rays; FASER (ForwArd Search ExpeRiment)  
 597 is another forward-based detector near ATLAS and searches for light, weakly interacting  
 598 particles; finally, MoEDAL (Monopole and Exotics Detector at the LHC) is installed in  
 599 proximity to LHCb and aims to detect magnetic monopoles and other exotic particles.

600 The technical design report for the LHC can be found at Ref. 32, detailing the ring itself,  
 601 infrastructure, general services, and the injector chain.

### 602 3.2.1 A proton's journey

603 A proton destined for the LHC begins its journey as a hydrogen atom in a little, red bottle.  
 604 Around  $3 \times 10^{14}$  protons are supplied to each beam in the LHC, with billions of refills  
 605 available in this single container. Once the hydrogen atoms leave the source, they are stripped  
 606 of their electrons, and [sent] to the linear accelerator LINAC2.<sup>1</sup> This is the start of a long  
 607 voyage through the accelerator complex (visualised in Fig. 3.1).

608 Given a modest boost to 50 MeV, the protons are sequentially fed from LINAC2 into  
 609 the Proton Synchrotron Booster (PSB) that accelerates them further to 1.4 GeV. Another

---

<sup>1</sup>As of the end of Run-2, LINAC2 has been decommissioned. It has been replaced by LINAC4 in preparation for Run-3.

upsurge is provided once the protons travel to the Proton Synchrotron (PS), this time to 26 GeV. Then, the final energy increase received before entering the LHC comes from the Super Proton Synchrotron (SPS), leaving the protons at 450 GeV. Once injected into the LHC, they are finally accelerated to their peak; up to 6.5 TeV from a sequence of radio frequency cavities over the course of twenty minutes. The oscillation frequency of these cavities is precisely tuned and timed to give protons the appropriate kicks and accelerate them to the desired energy. Since there is a distribution of proton energies in the beam, those that enter a cavity slightly out of time with a different energy than expected consequently become sorted into “bunches”. The remainder of the LHC ring is used to steer the beam with the aid of over 1,200 liquid helium-cooled superconducting dipole magnets. It is also focused by almost 400 equivalently-cooled quadrupole magnets to increase the rate of proton collisions.

One beam consists of a “train” of up to 2,808 bunches spaced 25 ns apart, each with 115 billion protons. Using bunches provides an advantage to the experiments at each of the interaction points. Discrete collisions take place between bunches in the opposing beams at 40 MHz as opposed to continuous streams of protons. This allows for estimates of pileup interactions that can be filtered out, and would otherwise introduce miscalculations of sums like  $p_T^{\text{miss}}$  and  $H_T$ . The data recorded by each experiment is naturally separated by the bunch crossing or event.

### 3.2.2 Luminosity

The *luminosity* of a particle accelerator is, along with centre of mass energy, a quantitative measure of its performance. It is often used to denote the amount of data delivered to, or collected by, the receiving detector. A full derivation of this quantity can be found in Ref. 71, and as such, only a summary is given here. The *instantaneous luminosity*  $\mathcal{L}$ , typically quoted in  $\text{cm}^{-2}\text{s}^{-1}$ , is defined as

$$(3.1) \quad \mathcal{L} = \frac{1}{\sigma_p} \frac{dN}{dt}$$

where  $N$  is the number of collisions and  $\sigma_p$  is the production cross section. In the LHC, because many final states are possible,  $\sigma_p$  is not generally known. It can be measured, however. A recent paper from LHCb measured the extrapolated inelastic cross section (which is the important component for LHC collisions) to be  $75.4 \pm 5.4 \text{ mb}$  at  $\sqrt{s} = 13 \text{ TeV}$  [6], allowing an estimate of the collision rate. For two colliding beams split into bunches with

### 3.2. THE LARGE HADRON COLLIDER

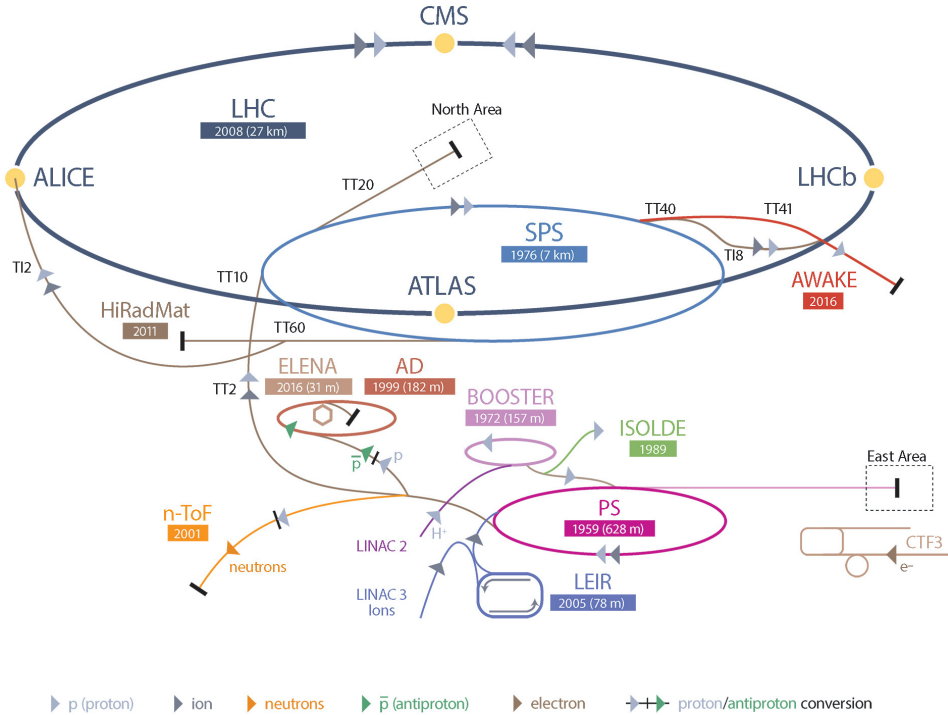


Figure 3.1: A schematic of the CERN accelerator complex. Various particles are shown from their sources to the detectors they are observed at. Figure obtained from Ref. 1.

the constituents in each bunch distributed according to a gaussian profile,

$$(3.2) \quad \mathcal{L} = \frac{N_1 N_2 f N_b}{4\pi\sigma_x\sigma_y} \cdot F$$

where  $N_1$  and  $N_2$  are the number of particles in a bunch in beams 1 and 2, respectively,  $N_b$  is the number of bunches per beam,  $f$  is the revolution frequency (11,245 Hz for protons in the LHC), and  $\sigma_x$  and  $\sigma_y$  are the horizontal and vertical sizes of the beam, respectively.<sup>2</sup>

The geometric reduction factor  $F$  is unity for beams colliding head on.<sup>3</sup> However, in the LHC, the beams collide at an angle known as the *crossing angle* to reduce the effects of pileup. At the start of a fill when the number of protons in the LHC is at its maximum, the crossing angle at each interaction point is approximately 300  $\mu$ rad. As the runs progress, more protons collide and the luminosity decreases. One of measures taken to recover luminosity and keep the LHC as efficient as possible is to reduce the crossing angle. By the end of the fill, it can be as small as 240  $\mu$ rad.

The instantaneous luminosity can be increased further by the inclusion of more bunches per beam, decreasing the size of a beam through improved quadrupole magnets, and by redu-

<sup>2</sup>Add the  $H$  factor from the hourglass effect and explain?

<sup>3</sup>Add mathematical formula for F?

642 cing the crossing angle. Tuning these parameters led the LHC to reach its design luminosity  
643 of  $10^{34} \text{ cm}^{-2} \text{ s}^{-1}$  in 2016. It had more than doubled by the end of Run-2.

Integrating the instantaneous luminosity over a period of time yields the *integrated luminosity*  $\mathcal{L}_{\text{int.}}$ :

$$(3.3) \quad \mathcal{L}_{\text{int.}} = \int \mathcal{L} dt$$

644 These values are often quoted by experiments in units of “inverse femtobarn” ( $\text{fb}^{-1}$ ) as an  
645 indicator of the amount of collision data collected. A “barn” is a unit equal to  $10^{-28} \text{ m}^2$   
646 and colloquially used to express cross sectional area in nuclear and particle physics. Thus  
647 its reciprocal, the same units as integrated luminosity, gives a good sense of scale that relates  
648 cross sections of individual processes to the total amount of data. Tab. 3.1 gives the integrated  
649 luminosities over Run-2 delivered by the LHC and collected by CMS. Taking  $137.19 \text{ fb}^{-1}$   
650 from this table, and assuming the inelastic  $pp$  cross section above gives an estimate of  $10^{16}$   
651 collisions recorded by CMS over Run-2 (excluding pileup interactions).

### 652 3.2.3 Pileup

653 At the high instantaneous luminosity of the LHC, multiple interactions per bunch crossing—  
654 known as *pileup*—are frequent. The expected, or nominal, number of collisions per bunch  
655 crossing is one, but because of all the factors that increase the luminosity, many “softer”  
656 collisions also take place. Pileup interactions can produce many low- $p_T$  objects, and near-  
657 collinear to the beam (detecting particles in this region is essential for some analyses). These  
658 additional objects can contaminate the reconstruction of the final state from the nominal  
659 collision, and as such affect the direction and magnitude of the  $\vec{p}_T^{\text{miss}}$ . When one aims to  
660 increase the luminosity to collect more data, the more severe pollution from pileup is an  
661 inevitable consequence. The distribution of pileup events in CMS during Run-2 can be seen  
662 in Fig. 3.2.

663 There are strategies in place in the LHC and the anchored experiments to mitigate pileup.  
664 Introducing, or increasing, a crossing angle between the beams reduces the effect. Track  
665 reconstruction algorithms are very efficient at connecting particles to their primary vertices,  
666 and therefore particles originating from pileup vertices can be identified and removed [2, 36].  
667 At CMS, various methods are available in the calorimeter triggers to subtract the effects of  
668 pileup.

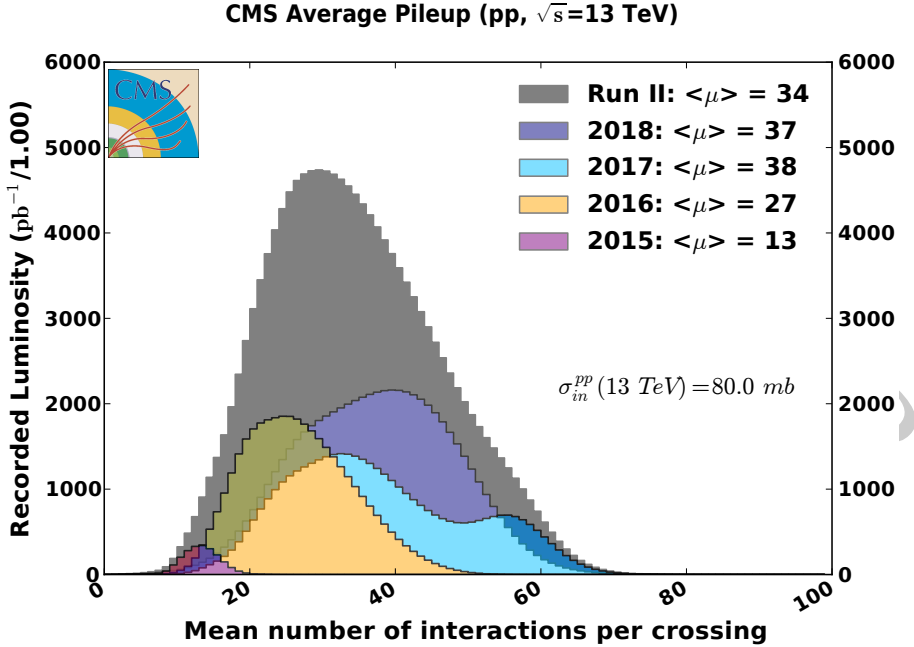


Figure 3.2: The average number of pileup interactions per bunch crossing at CMS during Run-2 of the LHC. Figure obtained from Ref. 42.

### 669 3.2.4 Evolution of the LHC

670 The LHC began operating in 2010 at a centre of mass energy of  $\sqrt{s} = 7 \text{ TeV}$ ;  $3.5 \text{ TeV}$  per  
 671 beam. A modest increase to  $8 \text{ TeV}$  was achieved by the end of Run-1 in 2013. Long Shutdown  
 672 1 then commenced where maintenance work was carried out, and upgrades to the accelerator  
 673 and experiments were performed. Notably, the superconducting magnets were improved to  
 674 safely handle much more energetic beams.

675 The LHC resumed operation in 2015, marking the start of Run-2 and further pushing the  
 676 frontiers of high energy physics with a centre of mass energy of  $\sqrt{s} = 13 \text{ TeV}$ . While valua-  
 677 ble data was taken that year, it was not until 2016 when substantial datasets were amassed.  
 678 Therefore, when analysts refer to the “full Run-2 dataset”, they typically do not include data  
 679 from 2015. It requires as much care as the other years with respect to implementing correc-  
 680 tions and addressing systematic uncertainties, and so on, for only a very small gain in integ-  
 681 rated luminosity. Run-2 ended in 2018 with—omitting the 2015 dataset— $158.64 \text{ fb}^{-1}$  of  $pp$   
 682 collisions delivered,  $146.45 \text{ fb}^{-1}$  of which were recorded by CMS who certified  $137.19 \text{ fb}^{-1}$   
 683 suitable for analysis [42, 43]. A breakdown by year is presented in Tab. 3.1<sup>4</sup> with a visual

<sup>4</sup> Maybe add Run-1 column(s)? One for  $7 \text{ TeV}$  (or 2011) and one for  $8 \text{ TeV}$  (or 2012)? Though, it does risk becoming too cluttered.

684 chart in Fig. 3.3.<sup>5</sup> By comparison, the LHC delivered only  $6.2 \text{ fb}^{-1}$  at 7 TeV and  $23.3 \text{ fb}^{-1}$  at  
 685 8 TeV over the course of Run-1.

Integrated luminosity	2015	2016	2017	2018	Full Run-2
Delivered by LHC ( $\text{fb}^{-1}$ )	4.21	40.99	49.79	67.86	162.85
Recorded by CMS ( $\text{fb}^{-1}$ )	3.80	37.80	44.98	63.67	150.25
Certified by CMS ( $\text{fb}^{-1}$ )	2.26	35.92	41.53	59.74	139.45

Table 3.1: The integrated luminosity delivered by the LHC during Run-2 which were recorded and certified by CMS. Typically, only the 2016–18 datasets are analysed since 2015 accrued little data compared to the other years. Numbers obtained from Refs. 42, 43.

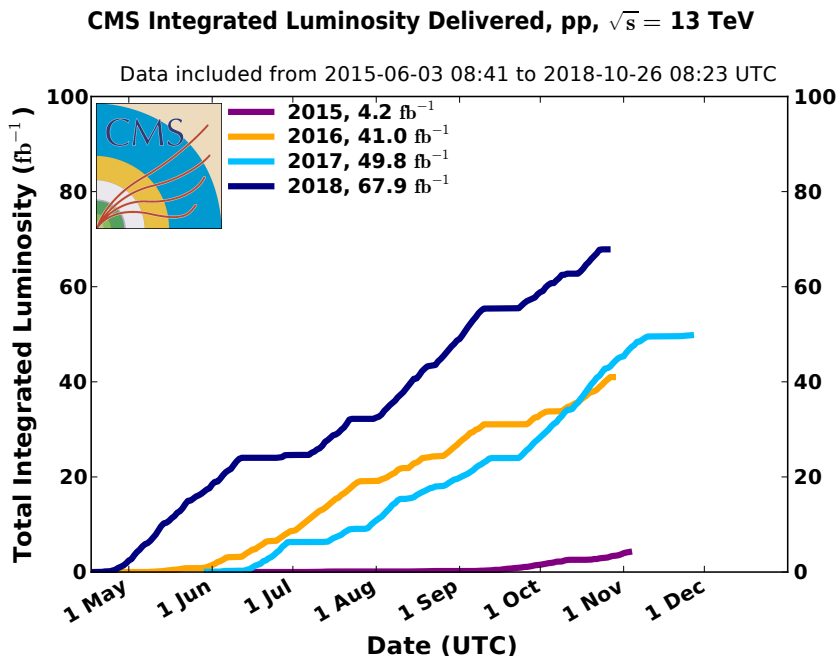


Figure 3.3: The integrated luminosity of  $pp$  collision data delivered to CMS during Run-2 of the LHC. Figure obtained from Ref. 42.

686 In addition to the upgrades that have so far been performed, a much grander change is  
 687 on the horizon. In 2027, the High Luminosity Large Hadron Collider (HL-LHC) improve-  
 688 ments are set to be introduced with the primary purpose of increasing the luminosity by up  
 689 to a factor of ten: more powerful magnets for focusing the beam, crab cavities for increas-  
 690 ing the bunch overlap area, shielding and more radiation-resistant components, an upgrade

<sup>5</sup>As I'm considering with the table, should I replace this figure with the one that also includes Run-1? But then there are lots of lines and things can look less clean.

691 to many of the boosters in the accelerator complex, and much more. A summary of the  
 692 important parameters at three stages of the LHC’s life is given in Tab. 3.2.<sup>6</sup>

Parameter	End of Run-2	HL-LHC	Design
Beam energy (TeV)	6.5	7	7
Bunches per beam	2,556	2,748	2,808
Protons per bunch	$1.5 \times 10^{11}$	$2.2 \times 10^{11}$	$1.5 \times 10^{11}$
Crossing angle ( $\mu\text{rad}$ )	300	590	285
Instantaneous luminosity ( $\text{cm}^{-2}\text{s}^{-1}$ )	$2.1 \times 10^{34}$	$7.2 \times 10^{34}$ *	$1.0 \times 10^{34}$
Integrated luminosity per year ( $\text{fb}^{-1}$ )	68	250	40
Average pileup per bunch crossing	34	140	27

Table 3.2: Some of the important parameters defining the performance of the LHC at the end of Run-2, for the High Luminosity Large Hadron Collider, and the design specification. Several values in this table were obtained from Refs. 14, 26.

\* Does not account for the large increase to virtual luminosity from the introduction of crab cavities.

### 693 3.3 The CMS experiment

694 The Compact Muon Solenoid (CMS) collaboration was formed in 1992 with a letter of in-  
 695 tent circulated to the high energy physics community for a general purpose detector to be  
 696 built at the LHC [51]. Though its emphasis was the detection of the Higgs boson, the myriad  
 697 avenues for which physics could be studied was also acknowledged. Just under five hundred  
 698 people from sixty two institutes were part of the original letter. At the time of writing over  
 699 five thousand physicists, engineers, technical and administrative staff, and students, span-  
 700 ning over two hundred institutes in fifty countries, comprise the collaboration. Working  
 701 tirelessly in harmony, with ingenuity, cooperation, and a drive for exploring the frontiers of  
 702 particle physics, almost one thousand publications have been produced with data collected  
 703 by the experiment. These range from exotic/BSM searches, standard model precision meas-  
 704 urements,  $B$ -physics, top quark physics, heavy ions, and more. This wide scope of topics  
 705 cements CMS as a versatile and world-leading detector, and collaboration as a whole.

---

<sup>6</sup>Should I add a column for the Tevatron, as a comparison to/sense of scale for the LHC’s numbers? Or maybe discuss the Tevatron qualitatively somewhere.

706 **3.3.1 The CMS detector**

707 The machine itself—aptly named the CMS Detector—lives a hundred metres underground at  
708 Interaction Point 5, just outside the town of Cessy in France. Constructed over several years,  
709 the detector was separated into fifteen sections. Each was built on the surface and lowered  
710 into the experimental cavern with an incredibly small tolerance of a few centimetres. Here,  
711 they were joined together to assemble the 14,000 tonne goliath. The finished detector is a  
712 hermetic cylinder enclosing the LHC beam pipe, measuring 21 m in length (plus a little extra  
713 from the bolt-on forward calorimeters) and 15 m in diameter. Its etymology stems from how  
714 *compact* (relatively speaking) the detector is since its weight is twice that of ATLAS in only  
715 one sixth of the volume, it has a subsystem dedicated to detecting *muons*, and a *solenoid* is  
716 used to generate the magnetic field.

717 CMS is designed to detect all manner of particles as accurately as possible. To accom-  
718 plish this, the detector is divided into four major subsystems (or subdetectors): the silicon  
719 tracker, the electromagnetic calorimeter (ECAL), the hadron calorimeter (HCAL), and the  
720 muon chambers. These are each explained in more detail below, with a graphic of the entire  
721 detector presented in Fig. 3.4 and a transverse slice through it in Fig. 3.6.

722 **3.3.1.1 Geometry**

Collider physics tends to use certain conventions when describing the positions of particles  
in a detector. The azimuthal angle  $\phi$  is the same variable as in cylindrical coordinates, i.e.,  
the angle subtended from the  $0^\circ$  direction on the polar axis to the particle’s position, with a  
range  $[-\pi, \pi]$ . Pseudorapidity, denoted by  $\eta$ , is a coordinate that describes the angle between  
a particle and the longitudinal axis of the detector (the beam line):

$$(3.4) \quad \eta = -\ln \left[ \tan \left( \frac{\theta}{2} \right) \right]$$

723 where  $\theta$  is the angle between the particle’s three-momentum  $\vec{p}$  and the positive direction of  
724 the beam axis. So as  $\theta \rightarrow 0^\circ$  (the beam line),  $\eta \rightarrow \infty$ . Generally, particles with large  $\eta$  escape  
725 the detector which is why forward calorimeters are in place. The transverse momentum of  
726 a particle can be found with  $p_T = |\vec{p}| / \cosh \eta$ .

727 The subdetectors of CMS are nominally separated into several sections dependent on  
728 their geometry or layout, and it is useful to divide them into  $\eta$  ranges to demonstrate their  
729 coverage. “Barrel” sections are cylindrical around the beam line while “end caps” are usually  
730 discs or plates perpendicular to it. The following subsections describe them in detail. One  
731 quadrant of CMS showing the  $\eta$  divisions can be seen in Fig. 3.5.

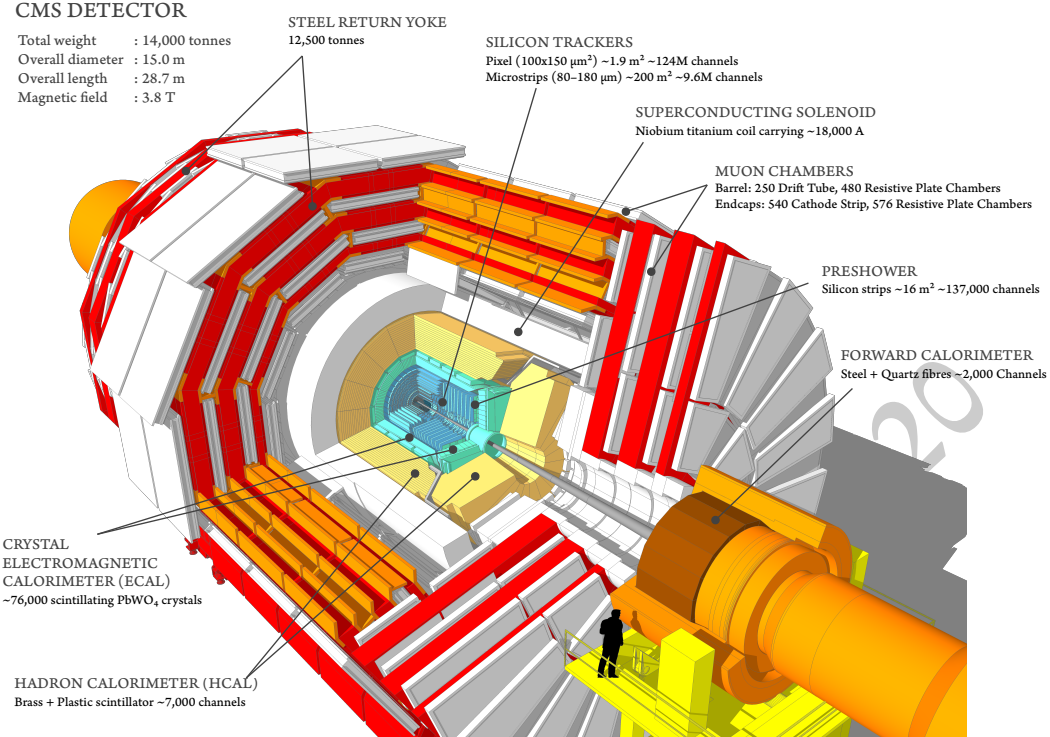


Figure 3.4: A cutaway diagram of the CMS detector with all of the principal components labelled. This detector configuration was used for the 2017–18 data taking years, where the coverage of the pixel detectors in the silicon tracker were upgraded. Image taken from Ref. 91.

The distance between two objects can be found with the variable  $\Delta R$ :

$$(3.5) \quad \Delta R = \sqrt{(\Delta\eta)^2 + (\Delta\phi)^2}$$

732 It is often used as a distance parameter in jet clustering, or between individual objects in  
733 highly-boosted decays.

### 734 3.3.1.2 The tracker

735 When a collision occurs, the ejected particles first encounter the silicon tracker that extends  
736 from 4 cm to just under 1 m in radius [48, 78]. Longitudinally, it is confined to  $|\eta| < 2.5$ ,  
737 known as the “central region”. The barrel and end cap sections are bound by  $|\eta| \lesssim 1.6$  and  
738  $1.6 \lesssim |\eta| < 2.5$ , respectively.

739 Consisting of tens of millions of pixels and microstrips, the positions of particles can be  
740 recorded to within  $10 \mu\text{m}$ . Initially, the pixel detector was arranged in three layers, covering  
741  $1 \text{ m}^2$  and consisting of 66 million channels. It was upgraded for the 2017–18 run period  
742 to introduce a fourth layer, increasing its coverage to  $1.9 \text{ m}^2$  with 124 million channels.

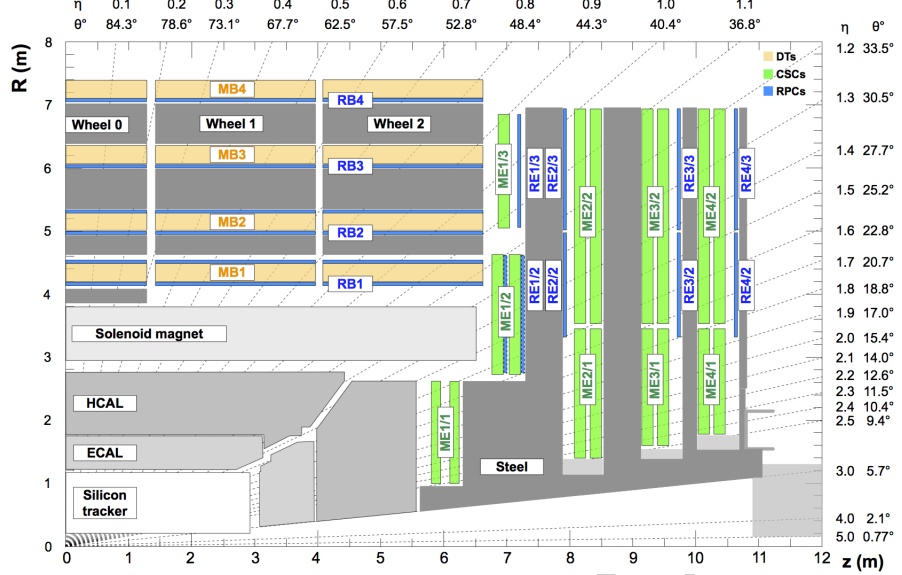


Figure 3.5: A quadrant of the CMS detector illustrating the main subsystems with their radius  $R$ , longitudinal distance  $z$ , and pseudorapidity  $\eta$  from the interaction point. The grey box at  $3 < |\eta| < 5$  and  $11 < z < 12$  m is the hadron forward calorimeter. Figure taken from Ref. 87.

743 The many layers of strip modules enclose the pixel detector. Since the tracker is the closest  
 744 subsystem to the interaction point, the components must be extremely radiation-tolerant to  
 745 withstand the bombardment of particles pummelling them every collision.

746 The hit is registered by a pixel or strip via electron-hole pairs created by the ionisation  
 747 caused from a particle interacting with the silicon. An electric field within the sensor separates  
 748 them and they drift toward the electrodes at the boundaries. The activity is then read  
 749 out, where pixels record electrons and strips record holes.

750 Track-finding algorithms use pattern recognition to determine whether the hits from  
 751 multiple layers in the tracker can be correlated and reconstructed to originate from individual  
 752 particles. Each is suited to different types of track,  $p_T$  threshold, and location. Vertex  
 753 reconstruction algorithms are employed to determine the primary vertex, and any secondary  
 754 (for example, in  $b$ -jets) or pileup vertices. The momentum of particles can be measured  
 755 from the curvature of the track from the magnetic field induced by the solenoid (see  
 756 Chpt. 3.3.1.5).<sup>7</sup>

<sup>7</sup>Should I mention something about resolution as well?

757 **3.3.1.3 The ECAL**

758 After the tracker, the particles can interact with the ECAL [29, 45]. The 76,000 lead-tungstate  
 759 crystals scintillate the incoming light, where the attached avalanche photodiodes record en-  
 760 ergy deposits in the barrel region ( $|\eta| < 1.48$ ) belonging to charged particles. Vacuum pho-  
 761 totriodes are instead glued to the crystals in the end caps ( $1.48 < |\eta| < 2.96$ ) as they are  
 762 subject to higher radiation doses. A lead-silicon preshower detector precedes the end cap  
 763 crystals to improve spatial resolution and discrimination of multiple particles. Electronics  
 764 for groups of  $5 \times 5$  crystals (the ECAL component of a “trigger tower”) read out the data  
 765 and deliver it to the trigger system (see Chpt. 3.3.2).

The ECAL is designed to identify charged particles, primarily electrons and photons. The  $H \rightarrow \gamma\gamma$  and  $H \rightarrow ZZ \rightarrow 4\ell$  processes were kept in mind, as an ardent focus was on discovering the Higgs boson. These particles are usually stopped entirely in the subdetector. Muons and tau leptons ( $\tau$ ), however, usually penetrate farther. Measuring the energy of electrons and photons is performed as follows:

$$(3.6) \quad E_{e,\gamma} = G(\eta) \cdot F_{e,\gamma} \cdot \sum_i A_i S_i(t) c_i$$

766 where  $G$  is the global energy scale,  $F$  is the cluster correction (as several hits in a cluster can  
 767 belong to one object, especially when they electromagnetically shower),  $A$  is the amplitude  
 768 of the pulse from the readout electronics,  $S$  is the time-dependent response correction from  
 769 the laser monitoring system that measures the crystal transparency, and  $c$  an intercalibration  
 770 correction that accounts for the non-uniform response of the crystals and photodetectors.<sup>8</sup>  
 771 Charged hadrons, muons and taus only deposit a sliver of energy in the ECAL, and so  
 772 information from the other subdetectors is required in their cases.

773 **3.3.1.4 The HCAL**

774 Hadronic particles propagate past the ECAL into the HCAL [46]. The barrel ( $|\eta| < 1.30$ )  
 775 and end cap ( $1.30 < |\eta| < 2.96$ ) regions both consist of brass absorber<sup>9</sup> and plastic scintil-  
 776 lator with wavelength-shifting fibre. Arranged in wedges in the barrel and discs in the end  
 777 cap, hybrid photodiodes record the signal in either case. This yields 7,000 detection chan-  
 778 nels. Due to colour confinement, hadrons are much more prone to showering than charged  
 779 leptons. Additional scintillator tiles are placed outside the yoke of solenoid in the barrel  
 780 region to capture the tails of these showers.

<sup>8</sup>Should I mention something about energy resolution as well?

<sup>9</sup>Famously, a large component of the brass used to build the end caps came from over 1 million decommissioned Russian naval artillery shells left over from World War II.

Unlike the ECAL which only covers the barrel and end cap, the HCAL also has a component in the forward region of the detector: the hadron forward calorimeter (HF). Composed of steel absorber and quartz fibres with 1,000 channels on each side, and occupying  $2.96 < |\eta| < 5.19$ ,<sup>10</sup> it is designed to detect particles with trajectories close to the beam line. The additional function of measuring the luminosity delivered to, and collected by, the experiment is also served. Cherenkov light kindled in the fibres is funnelled into photomultiplier tubes that collect the signal. Particles that enter the HF are usually not supplemented by tracker or ECAL information. As such, the energy and momentum of particles can be determined only by the subdetector.

Each cell of the HCAL maps onto a given number of ECAL crystals, forming trigger towers or calorimeter towers that are important when collecting data (see Chpt. 3.3.2). The towers project mostly-radially from the interaction point. Their granularity is greatest at low  $\eta$ , and decreases with increasing  $\eta$ . Information from both subdetectors is used to identify jets, muons, and taus, as well as any electrons or photons that penetrate through the ECAL. Readout electronics are mounted to the various components of the HCAL to deliver to the trigger system. The response and transparency of modules is corrected for in a similar way to the ECAL, as is intercalibration.

### 3.3.1.5 The magnet and muon chambers

The three subsystems described above are encased in a massive superconducting solenoid [47], making up 12,500 of the 14,000 tonne detector. It generates a magnetic field of 3.8 T and  $2.4 \times 10^9$  J of energy, making it the largest store of energy in the world for a single magnet. The field allows for the transverse momentum of a charged particle to be precisely measured, since the field propels it into a circular orbit. The magnetic force  $qvB$  exerted is equal to the centripetal force  $mv^2/r$ , and therefore the radius of the orbit is proportional to the momentum.

An iron return yoke interspersed with the muon chambers [83] constitute the rest of the detector, extending from a radius of around 3 m to 7.5 m. The iron yoke confines the magnetic field to the volume of the detector and provides a 2 T field in the opposite direction to that found farther inward. Since muons are much heavier than electrons and have high  $p_T$ , they penetrate farther than the bounds of the ECAL and deposit little energy in the process. The final states of several interesting decays include muons, such as with the Higgs boson. Consequently, constructing a dedicated subdetector is therefore essential.

---

<sup>10</sup>I'm not entirely sure what the bounds of the HF are. Literature seems to define it as  $3.0 < |\eta| < 5.0$ , but in the JEC the edge of the final  $|\eta|$  bin is 5.191.

813 There are four muon “stations”, as can be seen by the orange strips in Fig. 3.6, separated  
814 by layers of the return yoke. 480 resistive plate chambers and 250 drift tubes reside in the  
815 central barrel region of  $|\eta| < 1.2$ . The end caps are populated with 576 resistive plate cham-  
816 bers, complemented by 540 cathode strip chambers. Its limits are  $0.9 < |\eta| < 2.4$ , though  
817 the resistive plate chambers terminate at  $|\eta| = 1.9$ . Like many of CMS’ subdetector com-  
818 ponents, they are designed parallel and perpendicular to the beam line, not according to  $\eta$ .  
819 With such large segments at high radius in the muon chambers, a small overlap is therefore  
820 present. This  $0.9 < |\eta| < 1.2$  sector is sometimes referred to as the “overlap region”. The  
821 pseudorapidity range of the muon chambers’ end cap is restricted compared to the ECAL  
822 and HCAL to (mostly) align with the tracker, and the steel that surrounds the structure  
823 takes up the remainder of the  $\eta$  that the former two occupy.

824 All of the detectors in the muon chambers take advantage of gaseous ionisation, as it  
825 is much less expensive than the silicon used in the tracker while still providing excellent  
826 resolution. If a muon enters a cell in a drift tube or cathode strip chamber, its position can  
827 be measured by the length of time taken for the gas it ionises to drift to the anode wire of said  
828 cell in the presence of a strong electric field. The latter can additionally utilise the induced  
829 charge on the cathode strips for improved spatial resolution. The resistive plate chambers  
830 work on a similar principle, but use parallel plate capacitors and are predominantly used for  
831 timing purposes when the data is sent to the trigger system. To measure the momentum of  
832 the muons, information from both the tracker and muon detector are used where possible.<sup>11</sup>

### 833 3.3.2 Data acquisition and triggering

834 With the enormous collision rate at the CMS interaction point, acquiring data requires some  
835 thought and ingenuity. Today’s electronics cannot handle the bandwidth from recording  
836 every single collision,  $\mathcal{O}(1 \text{ petabyte s}^{-1})$ . As such, a *trigger* is used to select the events that  
837 may be of use to analysers. In CMS, a two stage trigger [24] is used: the Level-1 Trigger  
838 (L1T), implemented in the detector hardware; and the High-Level Trigger (HLT) [38], a  
839 software farm to further reduce the events selected at Level-1. The trigger is part of the larger  
840 data acquisition (DAQ) system. An intricate network of custom electronics and commer-  
841 cial processors—a union of hardware, firmware, and software—are interconnected by multi-  
842 gigabit links to record the products of the highest-energy manmade collisions on Earth.

---

<sup>11</sup>Maybe mention the upgrades done between Run-1 and Run-2 (each subsystem), and possibly even the planned upgrades for Run-3 and Phase-2.

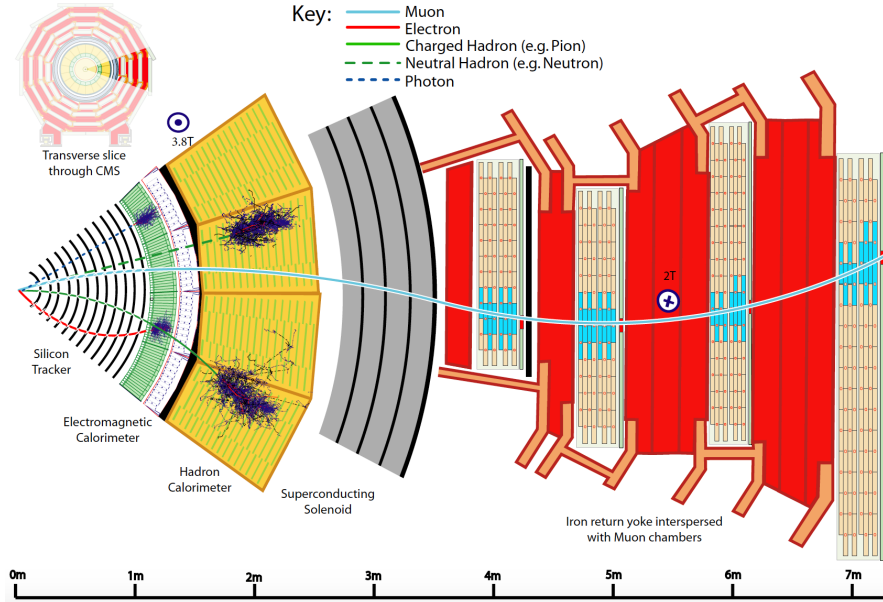


Figure 3.6: A transverse slice through the barrel section of the CMS detector with the main subsystems and components visible. Several particles produced at the primary vertex and their interactions with the detector are also depicted. Figure obtained from Ref. 94.

#### 843 3.3.2.1 The Level-1 Trigger

844 The Level-1 Trigger is a set of algorithms (a trigger menu)<sup>12</sup> implemented in custom hard-  
 845 ware designed to reduce the event rate from 40 MHz to a maximum of 100 kHz. FPGA  
 846 and ASIC chips contain the algorithms in firmware, with timing systems synchronised with  
 847 the LHC clock. When a collision occurs, particles interact with the detector and hits are  
 848 registered by the components.

849 Coarsely-segmented data is read out from the ECAL and HCAL through a two-layer  
 850 Calorimeter Trigger. These are arrays of custom processors located at Point 5. Layer-1 re-  
 851 ceives the calorimeter data from upwards of one thousand fibre optic links, each with multi-  
 852 gigabit bandwidths. The information from the two subsystems are combined into calori-  
 853 meter towers, and some simple position- and energy-dependent calibrations are applied.<sup>13</sup>  
 854 The data from Layer-1 is then transmitted to Layer-2, again over many high-bandwidth op-  
 855 tical links. Here, physics object candidates are identified ( $j$ ,  $e$ ,  $\gamma$ ,  $\tau$ ).<sup>14</sup> Additional cali-  
 856 brations are applied to them (for example, in Chpt. 3.3.4), and simple pileup subtraction is

<sup>12</sup>Do I need to say that different menus are used throughout the data-taking periods and for different injectants (heavy ions, etc.)?

<sup>13</sup>Mention something about trigger primitives here?

<sup>14</sup>An overview of the latest Run-2 algorithms for object identification can be found in Ref. 107.

857 performed.<sup>15</sup> Energy sums are also calculated at this stage, such as  $E_T^{\text{miss}}$ ,  $H_T$ , and  $H_T^{\text{miss}}$ .

858 In parallel, the various subdetectors in the muon chambers pass information through  
 859 successive stages, and is then combined with some of the calorimeter information in a sort-  
 860 ing/merging/isolation layer. The output from this layer is combined with the remaining  
 861 information within Layer-2 in the Global Trigger, a series of  $\mu$ TCA boards with FPGAs.  
 862 The trigger menu lives here, and all of the information gathered—object candidates, energy  
 863 sums, beam conditions—is provided to it. These triggers may be dependent on the presence  
 864 of a single object or the number of objects of a single class (e.g., one muon, two jets), multiple  
 865 classes of object (cross triggers), the energy sums, the topologies of objects, and more. The  
 866 latency given to make a decision on whether to keep or reject an event is 4  $\mu\text{s}$ .<sup>16</sup> A diagram  
 867 of this data flow is given in Fig. 3.7.

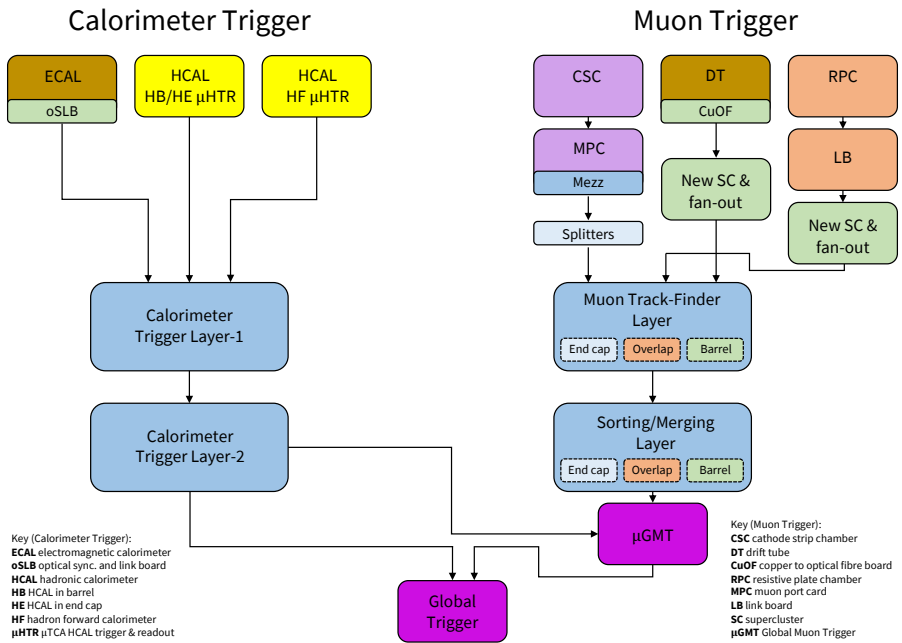


Figure 3.7: A summary of the CMS Level-1 Trigger data flow from the hits recorded by the subsystems to the Global Trigger. Figure reproduced from Ref. 52.

868 A small subset of data from the L1T is diverted for monitoring purposes. During data  
 869 taking periods, CMS has a plethora of members that participate in the supervision and main-  
 870 tenance of the experiment. At Point 5, shifters monitor the different domains, collecting  
 871 information from various sources. Data acquisition, data quality, access to the experimental

<sup>15</sup>Do I need to describe in detail how jets are formed? Jet seed, chunky donut PU subtraction, etc... Since it may be relevant for JEC.

<sup>16</sup>Mention pre-scaling of triggers, and that as  $\mathcal{L}$  decreases over a fill, the pre-scales change?

872 cavern, the L1T (which I have performed on numerous occasions), and the HLT are among  
873 them. Experts in these, and more specific systems, are on call on a rotating period. I, myself,  
874 have been an on call for Layer-2 of the Calorimeter Trigger several times.

875 **3.3.2.2 The High-Level Trigger**

876 Events that pass a logical OR of the triggers at Level-1 are transmitted to the HLT. The higher  
877 resolution data collected at the point of collision is available, along with information from  
878 the tracker. Populated with Intel Xeon processors (high core count CPUs), approximately  
879 22,000 cores are available (by the end of Run-2) to process the data sent from the L1T.  
880 In order to avoid a back-log, a 100 kHz input rate allows a HLT node  $\sim 220$  ms to make a  
881 decision. High-level software in the cmssw environment (written in C++ and Python, see  
882 Chpt. [REF]) is executed. A larger and more complex trigger menu is available, including  
883 the possibility analysis-specific triggers (such as those that target VBF topologies in Chpt. 4).  
884 Complex variables such as  $\alpha_T$  can even be calculated and triggered on.

885 Physics objects are reconstructed further, with algorithms such as anti- $k_T$  used to cluster  
886 jets [33]. Additional classification algorithms are also applied to objects, such as the DEEPCSV  
887 neural network to identify  $b$ -jets. A global event reconstruction from the PARTICLE FLOW al-  
888 gorithm (PF) [44, 94] is performed as well. Some of these algorithms can be computationally  
889 expensive. Consequently, only approximations/parametrisations are used at HLT level. The  
890 full-scale versions of these kind of algorithms are re-run on the retained events in later stages  
891 of postprocessing.<sup>17</sup>

892 The HLT reduces the event rate from the maximum 100 kHz input substantially to  
893 around 1 kHz. The data stream of  $\mathcal{O}(6 \text{ GB s}^{-1})$  is then subject to further processing be-  
894 fore the analysts access it. As well as the data being stored on networked hard drives at sites  
895 across the globe, back ups are made to magnetic tape for long term storage. As with the  
896 Level-1 Trigger, some data is redirected for monitoring, object calibrations, and alignment  
897 of detector components.

898 **3.3.3 Simulating CMS data**

899 Data recorded by CMS is paramount for analyses searching for new physics. However, sim-  
900 ulated samples are also of high importance. Events for specific processes are generated using  
901 Monte Carlo (MC) random sampling, and the output datasets are often collectively referred  
902 to by the method—“Monte Carlo” or “MC”. The datasets are often generated with large

---

<sup>17</sup>If more detail is required here, I should make a separate subsubsection and discuss.

903 numbers of events to minimise the associated statistical uncertainty. MC samples are useful  
904 in a variety of cases: understanding the kinematics of signal processes in searches for new  
905 physics, modelling background processes that can mimic signal, and comparisons to data for  
906 validation purposes.

907 A matrix element generator such as `MADGRAPH` [13] or `POWHEG` [62, 89] models the hard  
908 scattering process, usually at leading order (LO) but sometimes at higher orders. Events then  
909 pass through a hadroniser (usually `PYTHIA` [99] in CMS) to model hadronisation of quarks  
910 and gluons, sometimes known as the *parton shower*—the softer radiation that accompanies  
911 the hard scatter. Jets are clustered here by, for example, the anti- $k_T$  algorithm. The particles  
912 are also run through a detector simulation that emulates the configuration and response  
913 of the detector in different years. Material interactions and emulation of the triggers are in-  
914 cluded. `GEANT4` [9, 11, 12] provides this in CMS. Once the particles have been appropriately  
915 simulated, they are given the same postprocessing treatment as actual data, such as execut-  
916 ing object-tagging algorithms so that the data and simulated samples are as comparable as  
917 possible.

### 918 3.3.4 Jet energy corrections in the Level-1 Trigger

919 Recording the properties of hadrons that are amalgamated into jets is not always consistent  
920 across the detector. While the components go through quality control, there is inevitably  
921 some variation in their performance. They can degrade at different rates. Some may also  
922 receive hits more often than others and be subject to greater radiation damage. As a result,  
923 non-uniformity of the detector response—as functions of  $p_T$  and  $\eta$ —must be compensated  
924 for. For jets, this comes in the form of jet energy corrections (JEC).

925 As outlined in Chpt. 3.3.2.1, the trigger primitives from the ECAL and HCAL enter  
926 Layer-1 of the Calorimeter Trigger, where coarse position- and energy-dependent calibra-  
927 tions are applied. Objects such as jets are initially identified in Layer-2, and preliminary  
928 calibrations correct their energy. Disregarding these, even at this early stage in the data ac-  
929 quisition workflow, can affect the efficiency and rate of the Level-1 Trigger. It is therefore  
930 important to re-derive the calibrations regularly, since the configuration of the detector and  
931 beam conditions change over the lifetime of the experiment.

932 When a new round of calibrations are derived, there are many steps before this one.  
933 Preceding it, Layer-1 experts calculate their scale factors for the calorimeter towers. Once  
934 performed, the jet energy corrections are then derived in `cmssw`. The repository is accessible

935 at <https://github.com/eshwen/L1JetEnergyCorrections>.<sup>18</sup>

936 **3.3.4.1 The procedure**

937 QCD multijet MC datasets with a large  $p_T$  range used to derive the Layer-1 and Layer-  
 938 2 calibrations. Corresponding jets in data for this process can often be mismeasured (so  
 939 providing good calibrations in the most difficult scenario is a good test), and MC events  
 940 contain “truth-level” information from the generator. Ntuples are made from these which  
 941 have the Layer-1 corrections applied. Referring to the processing chain in Chpt. 3.3.3, the  
 942 jets these calibrations are derived for are post-hadronisation, but before interaction with the  
 943 detector. They will be referred to as “Level-1 (L1) jets”. The reference jets directly from the  
 944 generator (“GenJets” as colloquialised in CMS) are important for matching to our L1 jets to  
 945 ensure we are not mistakenly using jets from the parton shower that have no well-defined  
 946 source.

947 The reference and L1 jets are matched using the variable  $\Delta R$  (see Eq. 3.5). The algorithm  
 948 used to match the jets does so by inspecting each L1 jet in descending  $p_T$  and searching for  
 949 a reference jet with  $\Delta R < 0.25$ . If there is more than one match, the reference jet with the  
 950 smallest  $\Delta R$  is taken. Then the next L1 jet (and so on) follows the same procedure, with the  
 951 previous reference jet removed from the matching collection.

The pairs of jets are categorised into sixteen bins of  $|\eta|$ , the highest granularity available  
 since the calibrations must run quickly on hardware. Each bin is then analysed in turn.  
 Within each  $|\eta|$  bin, the jet pairs are subdivided into bins of the transverse momentum of  
 the reference jet ( $p_T^{\text{ref.}}$ ).<sup>19</sup> The bin widths, like  $|\eta|$ , are variable. The ratio of the transverse  
 momentum of the L1 jet ( $p_T^{\text{L1}}$ ) to  $p_T^{\text{ref.}}$  is taken for each pair of jets. Our metric for measuring  
 the detector response is the mean of these ratios:

$$(3.7) \quad r_j = \langle p_T^{\text{L1}} / p_T^{\text{ref.}} \rangle$$

The reciprocal of  $r_j$  vs.  $p_T^{\text{L1}}$  is inspected and a correction curve is fitted. A gaussian captures  
 the peak at low  $p_T$  and the following equation<sup>20</sup> is used for the tail:

$$(3.8) \quad p_T^{\text{L1, corr.}} = p_T^{\text{L1}} \cdot \left( p_0 + \frac{p_1}{\left( \log_{10} p_T^{\text{L1}} \right)^2 + p_2} + p_3 \cdot \exp \left( -p_4 \left( \log_{10} p_T^{\text{L1}} - p_5 \right)^2 \right) \right)$$

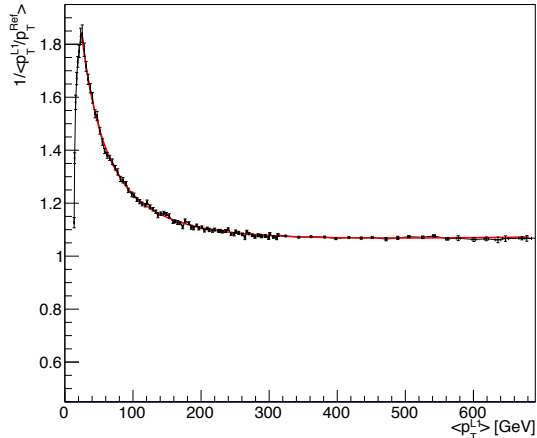
---

<sup>18</sup>Note: I have only forked it from the original developers and made modifications on top.

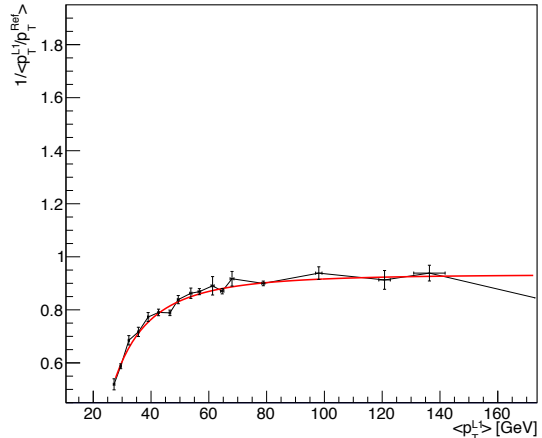
<sup>19</sup>Should I add tables somewhere of the  $p_T^{\text{ref.}}$  and  $|\eta|$  bins for the calibrations?

<sup>20</sup>Go into more detail regarding the equation? Reasoning, etc.

952 The input parameters for the function may not be adequate for all cases, so they are often  
 953 tuned to capture the low- $p_T$  spike and high- $p_T$  plateau (see Fig. 3.8 for an example). The  
 954 value of this fit function in each  $p_T^{\text{ref}}$  bin is exported.



(a)  $0.435 < |\eta| < 0.783$  (Barrel)



(b)  $4.191 < |\eta| < 5.191$  (HF)

Figure 3.8: Examples of correction curves used to calibrate the jet energies in two  $|\eta|$  bins. The reciprocal of the response is plotted against the  $p_T$  of the Level-1 jet, and a complex function (Eq. 3.7) fits the points. These plots are from the jet energy corrections performed on 2018 QCD Monte Carlo.

955 Once all  $|\eta|$  bins have been inspected, the calibrations are consolidated in several forms.  
 956 A machine-readable lookup table is included in the firmware of the Layer-2 hardware, so that  
 957 the corrections are applied in the trigger. A version is added to the Level-1 Trigger packages  
 958 in CMSSW so that the next steps in the calibration chain can utilise them.

959 A closure test is conducted to validate the corrections we have just produced. The MC  
 960 ntuples are regenerated with the JEC applied. Jet matching is performed and the calibrations  
 961 are checked. Many diagnostic and performance plots are produced to ensure the calibrations  
 962 are functioning as expected. These can be inclusive of the number of pileup interactions, or  
 963 split into ranges to see if the calibrations differ between them. Examples of these are Fig. 3.9  
 964 showing scatter plots of  $p_T^{\text{ref}}$  vs.  $p_T^{\text{L1}}$  before and after JEC are applied, and Fig. 3.10 illustrating  
 965 the response.

CHAPTER 3. THE LHC AND THE CMS EXPERIMENT

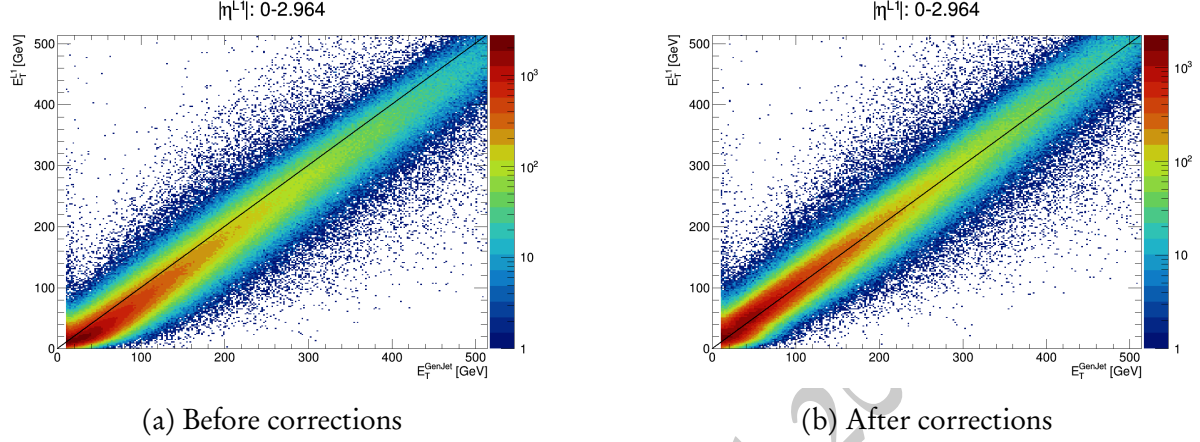


Figure 3.9: The energies of matched pairs of jets in the entire barrel and end cap, in the pileup 40–50 range, before and after jet energy corrections have been applied. After calibrations, the distribution is much more symmetrical. An equivalent plot using jets from LHC data is expected to look similar after applying these calibrations.

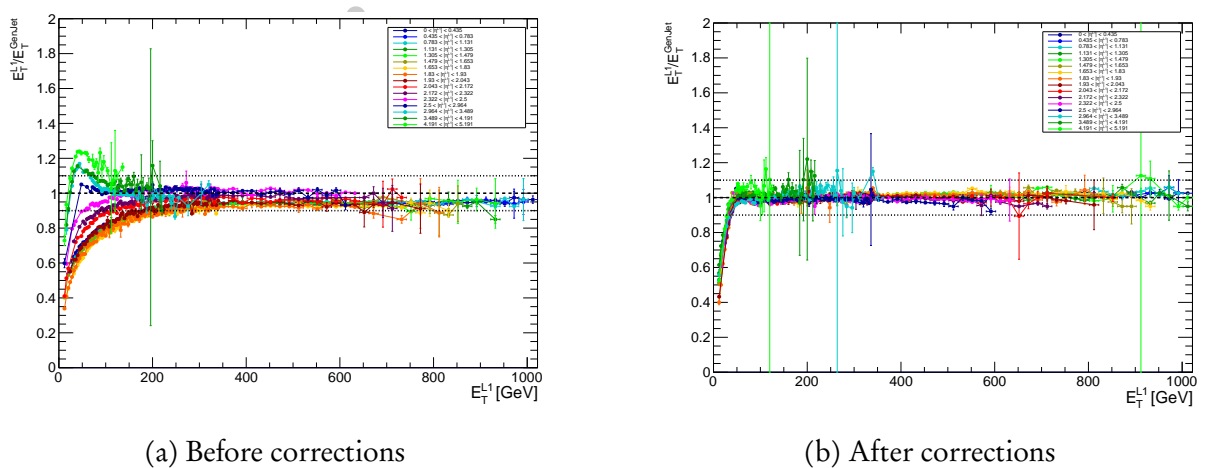


Figure 3.10: The response curves in each  $|\eta|$  bin as a function of  $p_T^{\text{L1}}$ , in the pileup 40–50 range, before and after JEC are applied. Note that in panel b, the  $x$ -axis is the corrected  $p_T^{\text{L1}}$ .

966

967

## COMBINED SEARCH FOR INVISIBLY DECAYING HIGGS BOSONS IN HADRONIC CHANNELS

969 This is the analysis chapter on  $H \rightarrow \text{inv.}$ .  
970 - Discuss how the theoretical aspects from the Theory chapter translate into an exper-  
971 imental search.

- 972 - Discuss the necessity of including all production modes of Higgs (invisible final state,  
973 so characterise events based on initial/additional particles). Also mention how sensitive  
974 each production mode is at contributing to the branching ratio limit. Emphasise the  
975 non-VBF modes ( $ggF$ ,  $t\bar{t}H$ ,  $VH - W^+H$ ,  $W^-H$ ,  $ZH$ ) in this chapter as that's what  
976 I've been working on and another student will be covering VBF.
- 977 - Add a section or subsection somewhere regarding analysis tools. Perhaps add a brief  
978 description of ROOT (and how it's entrenched in HEP even though people are tending  
979 to move away from ROOT-based analysis onto more industry-standard tools), then lead  
980 into the FAST tools and using dataframes, vectorisation, etc., with only small interfaces  
981 to ROOT (for I/O) to extract data. Potentially mention how the data tiers work in CMS  
982 (RAW, DIGI, RECO, AOD, miniAOD, nanoAOD, etc.)
- 983 - Talk about what makes this analysis unique: doing a combination over all production  
984 modes from the start instead of separate analyses combined at the end.
- 985 • Means we can share samples, systematics, background methods and workflows,  
986 build in orthogonality between the different modes, simultaneously optimise the  
987 categories for different production modes, and cover as much phase space as pos-

988           sible (with new final states such as boosted  $Z$  bosons with unresolved subjets).  
989           This makes the analysis much more cohesive and consistent.

990           – Include object definitions, overall analysis strategy, triggers, signal production (with  
991           each non-VBF mode in detail), event selection, background estimation (control re-  
992           gions, sidebands) and results/limit (including comparisons to previous results).

993           – Emphasise my contributions: control region construction and studies, background es-  
994           timation, and other studies I will have conducted by the time I write up.

995           – Current material: no public plots as of yet. Hope to finish analysis soon. We are pre-  
996           paring a CMS internal analysis note, documenting all aspects of the analysis. I will  
997           first add all relevant information there which I can subsequently use when writing this  
998           chapter.

999           – Since it's my thesis, I can talk about  $t\bar{t}H$ ,  $VH$  and  $ggF$ /monojet, even though the  
1000           Bristol contribution to the final, public result would only be  $t\bar{t}H$  and resolved  $VH$ .  
1001           Would need to be able to run the fit for all three modes simultaneously, ensuring we  
1002           have complete (and correct) systematics for  $ggF$ .

1003 **4.1 Analysis overview**

1004 **4.1.1 Hadronic production modes of the Higgs boson**

1005 **4.2 Categorisation of the non-VBF production modes**

1006 **4.3 Data and simulation**

1007 **4.3.1 Weights and corrections for simulated processes**

1008 In order for simulated events, particularly for background processes, to resemble LHC data  
1009 as closely as possible, many corrections and weights are applied.<sup>1</sup> These are discussed in  
1010 more detail in the following sections [REF]. A final event weight  $w_{\text{event}}$  is the product of  
1011 the weights from all of the individual sources  $i$  that provide one:

$$(4.1) \quad w_{\text{event}} = \prod_i w_i$$

---

<sup>1</sup>The following stuff on weights is from what I wrote in the AN. But it may be too detailed/unnecessary for that document, so I've made a copy here in case it is removed from there.

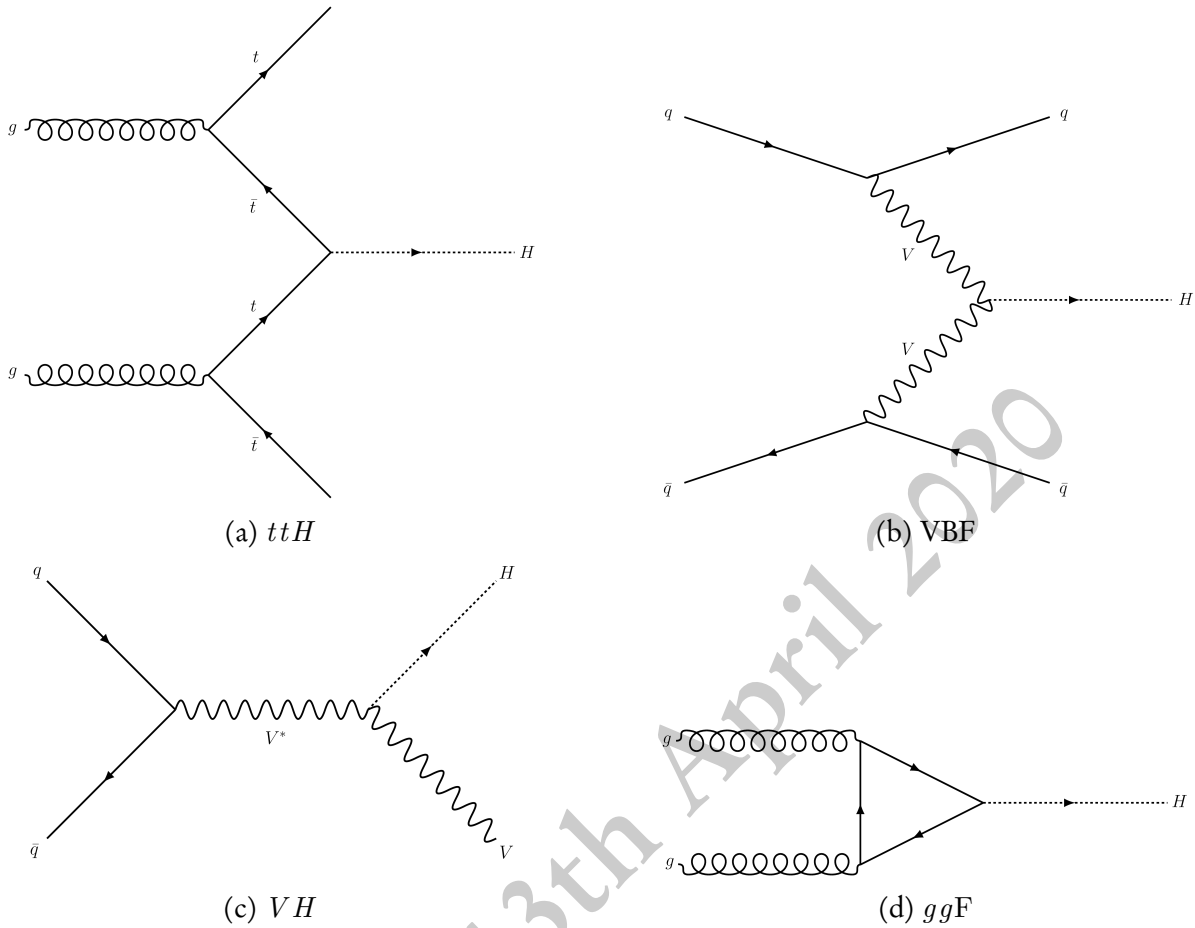


Figure 4.1: The Feynman diagrams for the four main hadronic production modes of the Higgs boson.

1012 When representing these events in histograms, the yield in a given bin  $N_{\text{corr.}}$  is the sum  
 1013 of these event weights:

$$(4.2) \quad N_{\text{corr.}} = \sum_j^{N_{\text{MC}}} w_{\text{event } j}$$

1014 where  $N_{\text{MC}}$  is the number of unweighted, simulated events in the bin. The statistical  
 1015 uncertainty ascribed to the yield in a bin is given as

$$(4.3) \quad \Delta N_{\text{corr.}} = \pm \frac{N_{\text{corr.}}}{\sqrt{N_{\text{MC}}}}$$

1016 The statistical uncertainty for the number of events in data is simply the Poissonian  
 1017 error,

$$(4.4) \quad \Delta N_{\text{data}} = \pm \frac{N_{\text{data}}}{\sqrt{N_{\text{data}}}}$$

1018 The standard prescription for error propagation is to approximate the uncertainty as the  
1019 square root of the sum of the weights squared [27]:

$$(4.5) \quad \Delta N_{\text{corr.}} = \pm \left( \sum_j^{N_{\text{MC}}} w_{\text{event } j}^2 \right)^{1/2}$$

1020 Our reasoning for using Eq. 4.3 for MC instead of Eq. 4.5 is that the error should be  
1021 determined purely from the integer number of events we select ( $k$  in a Poisson statistical  
1022 treatment), regardless of whether they are weighted or not. This often reduces the uncer-  
1023 tainty for MC compared to Eq. 4.5 since many more events are generated to predict a given  
1024 equivalent luminosity. Further justification is that it is a good approximation in our assumed  
1025 regime where we expect a large number of events from our MC samples before any cuts are  
1026 applied (say  $N$ ), and a large enough number of events after the cuts such that we do not  
1027 encounter the low- $k$  or low- $N$  limits of Poissonian error propagation.

1028 **4.3.1.1 Cross section reweighting**

1029 Since an arbitrary number of events can be generated for simulation, and a larger number  
1030 of events gives higher statistical power, events in these datasets need to be reweighted to  
1031 normalise their presence in a given region or category. To first order, the weight applied is

$$(4.6) \quad w_\sigma = \frac{\sigma \mathcal{L}_{\text{int.}}}{N \varepsilon}$$

1032 where  $\sigma$  is the cross section of the process at the order it was generated,  $\mathcal{L}_{\text{int.}}$  is the  
1033 integrated luminosity of the LHC data it is being compared to,  $N$  is the number of events in  
1034 the dataset before any analysis-level cuts are applied (or the sum of the generator weights),  
1035 and  $\varepsilon$  is the filter efficiency (assumed to be unity for all datasets since no generator-level cuts  
1036 are applied). If a dataset is generated at leading order, higher order corrections are usually  
1037 applied on an event-by-event basis that changes the shapes of distributions (see [SEC ON  
1038 NLO CORRECTIONS]). In some circumstances, “flat” k-factors can be applied to a dataset  
1039 that only alters the normalisation (i.e., its cross section).

1040 **4.3.1.2 Pileup reweighting**

1041 Pileup interactions at the LHC are frequent (see Chpt. 3.2.3) and must be modelled appro-  
 1042 priately in simulation. Simulated samples are generated with a certain distribution of the  
 1043 number of pileup interactions which usually does not match the data recorded by CMS.  
 1044 This is due to changing conditions in the beam over a period of data taking. In order to  
 1045 make them comparable, the simulated events are reweighted; in this context it is known as  
 1046 *pileup reweighting*. ROOT files containing histograms of the number of pileup interactions  
 1047 from short runs in the LHC are available centrally and are used as the reference for which  
 1048 to reweight the simulated events.

1049 In the trees of the simulated samples, the branch `Pileup_nTrueInt` is the mean of the  
 1050 Poisson distribution from which random numbers are drawn. In each simulated event, these  
 1051 random numbers (all from the same distribution) are used to set the number of in-time  
 1052 pileup interactions as well as the number of the interactions in each neighbouring bunch  
 1053 crossing to simulate the out-of-time pileup. In data, the same branch gives the average num-  
 1054 ber of pileup interactions for a colliding bunch pair in a lumi section. The distribution of  
 1055 `Pileup_nTrueInt` in the data is derived from the measured instantaneous luminosity for  
 1056 each colliding bunch pair in each lumi section and the cross section of the total inelastic  $p\bar{p}$   
 1057 interaction.<sup>2</sup>

1058 The nominal pileup weight for each simulated event, as well as the up and down system-  
 1059 atic variations, are derived in NANOAOD-TOOLS.

1060 **4.3.1.3 Veto and selection weights**

1061 In an analysis, events are often rejected by placing kinematic or object-based requirements.  
 1062 This type of selection strictly removes an event from the analysis if the requirement is not  
 1063 met. While kinematic requirements are either fulfilled or not, a different approach can be  
 1064 used when selecting the number of objects, i.e., when defining control regions. For a set of  
 1065 objects, the selection weight at event level is defined as

$$(4.7) \quad w_{\text{sel.}} = \prod_i^{N_{\text{objects}}} \epsilon_i$$

1066 where  $\epsilon_i$  is the efficiency/scale factor applied to object  $i$ . Only reconstructed (“reco  
 1067 level”) objects that have been matched to a generator level object are considered. For leptons

---

<sup>2</sup>Add a note about the min bias cross sections from the samples used to derive the data distributions for each year?

(e,  $\mu$ ,  $\tau$ ) and photons, these scale factors are typically from the reconstruction efficiency, identification efficiency, and  $p_T$ - or  $\eta$ -dependent energy corrections. In the case of  $b$ -tagged jets, it is the data-MC scale factor at the given working point of the algorithm used to identify them. These weights are calculated individually for each type of object in an event, and individually for each source since they also introduce systematic variations that cannot be trivially aggregated. A veto weight is defined as

$$(4.8) \quad w_{\text{veto}} = \prod_i^{N_{\text{objects}}} 1 - \epsilon_i$$

The uncertainties/systematic variations follow the same prescription. With these quantities defined, an event that meets the object criteria is given the selection weight, otherwise it is given the veto weight. For example, if an event with one muon meets the criteria for the  $\mu + \text{jets}$  region, it will enter that region with its muon-related selection weights. That same event can also enter the signal region or one of the sidebands (depending on the event kinematics) with the veto weights of the other objects. This “migration” of events, where they are able to contribute to more than one region, and the fact that weights are applied instead of event rejection, provides a noticeable decrease to the Monte Carlo statistical uncertainty in a given bin of a distribution.

One thing must be noted about the migration of events, since we have many different regions of phase space in the analysis. The signal region and the sidebands have orthogonal kinematic requirements, so an event cannot enter the signal region *and* one of the sidebands. The same is true amongst the control regions, i.e., an event cannot enter more than one of them due to the designed orthogonality. An event *is* able to enter the signal region or a sideband with  $w_{\text{veto}}$ , and also one of the control regions with  $w_{\text{sel}}$ . Since events in data are not weighted, they may only enter a single region.

## 1090 4.4 Triggers

## 1091 4.5 Background estimation

### 1092 4.5.1 Control regions

### 1093 4.5.2 Sidebands to the signal region

### 1094 4.5.3 Background estimation methods

1095

1096 SEARCH FOR DARK MATTER THROUGH THE PRODUCTION OF  
1097 SEMI-VISIBLE JETS

1098 This is the analysis chapter on semi-visible jets.

1099 – Discuss how the theoretical aspects from the Theory chapter translate into an exper-  
1100 imental search.1101 – Include object definitions, triggers, overall analysis strategy, signal production, event  
1102 selection, background estimation and results/limit (including comparisons to similar  
1103 searches – monojet/dijet exotic searches). Go through everything as more of a sum-  
1104 mary/overview rather than describing everything in as much detail as Higgs to invis-  
1105 ible.1106 – Emphasise my contributions:  $s$ - and  $t$ -channel signal model production and under-  
1107 standing. Angular variable study for QCD background rejection (if used).1108 – Current material: no public plots as of yet. Hope to finish  $s$ -channel analysis soon (see  
1109 previous section for caveats regarding inclusion), no timeline on  $t$ -channel or boosted  
1110  $Z'$  analysis.

1111 **5.1 Analysis overview**

1112 **5.2 Data and simulation**

1113 **5.2.1 Generating signal samples in PYTHIA**

1114 **5.2.2 Generating signal samples in MADGRAPH**

1115 **5.2.3 Triggers**

1116 **5.3 Background estimation**

1117

1118

## CONCLUSIONS

1119 This is the conclusion.

1120 – Include a summary of thesis and work done over the course of my PhD with emphasis  
1121 on the most important results/contributions.1122 – Mention the direction the semi-visible jet and Higgs to invisible analyses can take (sharing  
1123 ideas/strategies I have, potential improvements with more LHC data and future  
1124 prospects from potential future experiments).1125 • SVJ has the  $t$ -channel and boosted searches underway, so those could yield inter-  
1126 esting results. Long-lived searches are also an option. Higher energy collider like  
1127 FCC gives larger range of phase space to explore.1128 • For Higgs to invisible, precision collider like FCC-ee or ILC might be required  
1129 to actually observe the process (assuming its  $\mathcal{B}$  is around SM value). Otherwise,  
1130 we just need a lot of LHC data to narrow down the  $\mathcal{B}$  if it is enhanced by some  
1131 BSM process.1132 • Both searches can be improved with better ML techniques and stuff for categor-  
1133 isation/background rejection.

Draft: 13th April 2020



1134

1135

1136      B egins an appendix. Currently just a placeholder for any appendices that I plan to  
1137 include.

Draft: 13th April 2020

## BIBLIOGRAPHY

- 1139 [1] S.(UKRI), *CERN Accelerator Complex*, URL: <https://stfc.ukri.org/research/particle-physics-and-particle-astrophysics/large-hadron-collider/cern-accelerator-complex/> (visited on 22/03/2020).
- 1140  
1141  
1142 [2] M. AABOUD et al., *Performance of the ATLAS Track Reconstruction Algorithms in Dense Environments in LHC Run 2*, Eur. Phys. J. C77.10 (2017), p. 673, DOI: 10.1140/epjc/s10052-017-5225-7, arXiv: 1704.07983 [hep-ex].
- 1143  
1144  
1145 [3] M. AABOUD et al., *Combination of searches for invisible Higgs boson decays with the ATLAS experiment*, Submitted to: Phys. Rev. Lett. (2019), arXiv: 1904.05105 [hep-ex].
- 1146  
1147  
1148 [4] M. AABOUD et al., *Observation of  $H \rightarrow b\bar{b}$  decays and  $VH$  production with the ATLAS detector*, Phys. Lett. B786 (2018), pp. 59–86, DOI: 10.1016/j.physletb.2018.09.013, arXiv: 1808.08238 [hep-ex].
- 1149  
1150  
1151 [5] G. AAD et al., *Observation of a new particle in the search for the Standard Model Higgs boson with the ATLAS detector at the LHC*, Phys. Lett. B716 (2012), pp. 1–29, DOI: 10.1016/j.physletb.2012.08.020, arXiv: 1207.7214 [hep-ex].
- 1152  
1153  
1154 [6] R. AAIJ et al., *Measurement of the inelastic  $pp$  cross-section at a centre-of-mass energy of 13 TeV*, JHEP 06 (2018), p. 100, DOI: 10.1007/JHEP06(2018)100, arXiv: 1803.10974 [hep-ex].
- 1155  
1156  
1157 [7] D. ABERCROMBIE et al., *Dark Matter Benchmark Models for Early LHC Run-2 Searches: Report of the ATLAS/CMS Dark Matter Forum*, Phys. Dark Univ. 27 (2020), ed. by A. BOVEIA et al., p. 100371, DOI: 10.1016/j.dark.2019.100371, arXiv: 1507.00966 [hep-ex].
- 1158  
1159  
1160  
1161 [8] N. AGHANIM et al., *Planck 2018 results. VI. Cosmological parameters* (2018), arXiv: 1807.06209 [astro-ph.CO].

## BIBLIOGRAPHY

---

- 1163 [9] S. AGOSTINELLI et al., *Geant4—a simulation toolkit*, Nuclear Instruments and Meth-  
1164 ods in Physics Research Section A: Accelerators, Spectrometers, Detectors and As-  
1165 sociated Equipment 506.3 (2003), pp. 250–303, ISSN: 0168-9002, DOI: [https://doi.org/10.1016/S0168-9002\(03\)01368-8](https://doi.org/10.1016/S0168-9002(03)01368-8).
- 1167 [10] D. S. AKERIB et al., *The LUX-ZEPLIN(LZ) Experiment*, Nucl. Instrum. Meth. A953  
1168 (2020), p. 163047, DOI: 10.1016/j.nima.2019.163047, arXiv: 1910.09124  
1169 [physics.ins-det].
- 1170 [11] J. A. et. al., *Recent developments in Geant4*, Nuclear Instruments and Methods in  
1171 Physics Research Section A: Accelerators, Spectrometers, Detectors and Associated  
1172 Equipment 835 (2016), pp. 186–225, ISSN: 0168-9002, DOI: <https://doi.org/10.1016/j.nima.2016.06.125>.
- 1174 [12] J. ALLISON et al., *Geant4 developments and applications*, IEEE Transactions on Nu-  
1175 clear Science 53.1 (Feb. 2006), pp. 270–278, ISSN: 1558-1578, DOI: 10.1109/TNS.  
1176 2006.869826.
- 1177 [13] J. ALWALL et al., *The automated computation of tree-level and next-to-leading order  
1178 differential cross sections, and their matching to parton shower simulations*, JHEP 07  
1179 (2014), p. 079, DOI: 10.1007/JHEP07(2014)079, arXiv: 1405.0301 [hep-ph].
- 1180 [14] G. APOLLINARI et al., *High Luminosity Large Hadron Collider HL-LHC*, CERN  
1181 Yellow Rep. 5 (2015), pp. 1–19, DOI: 10.5170/CERN-2015-005.1, arXiv: 1705.  
1182 08830 [physics.acc-ph].
- 1183 [15] G. ARCADI, A. DJOUADI and M. RAIDAL, *Dark Matter through the Higgs portal*, Phys.  
1184 Rept. 842 (2020), pp. 1–180, DOI: 10.1016/j.physrep.2019.11.003, arXiv:  
1185 1903.03616 [hep-ph].
- 1186 [16] G. ARNISON et al., *Experimental observation of isolated large transverse energy electrons  
1187 with associated missing energy at  $\sqrt{s} = 540 \text{ GeV}$* , Physics Letters B 122.1 (1983),  
1188 pp. 103–116, ISSN: 0370-2693, DOI: [https://doi.org/10.1016/0370-2693\(83\)91177-2](https://doi.org/10.1016/0370-2693(83)91177-2).
- 1190 [17] G. ARNISON et al., *Experimental Observation of Lepton Pairs of Invariant Mass Around  
1191 95-GeV/c\*\*2 at the CERN SPS Collider*, Phys. Lett. 126B (1983), pp. 398–410, DOI:  
1192 10.1016/0370-2693(83)90188-0.
- 1193 [18] P. ATHRON et al., *Global analyses of Higgs portal singlet dark matter models using  
1194 GAMBIT*, The European Physical Journal C 79.1 (2019), p. 38, DOI: 10.1140/  
1195 epjc/s10052-018-6513-6.

- 1196 [19] P. BAGNAIA et al., *Evidence for  $Z0 \rightarrow e^+ e^-$  at the CERN anti- $p\ p$  Collider*, Phys.  
 1197 Lett. 129B (1983), pp. 130–140, DOI: 10.1016/0370-2693(83)90744-X.
- 1198 [20] I. BALDES and K. PETRAKI, *Asymmetric thermal-relic dark matter: Sommerfeld-enhanced  
 1199 freeze-out, annihilation signals and unitarity bounds* (2017), arXiv: 1703.00478  
 1200 [hep-ph].
- 1201 [21] M. BANNER et al., *Observation of single isolated electrons of high transverse momentum  
 1202 in events with missing transverse energy at the CERN pp collider*, Physics Letters B  
 1203 122.5 (1983), pp. 476–485, ISSN: 0370-2693, DOI: [https://doi.org/10.1016/0370-2693\(83\)91605-2](https://doi.org/10.1016/0370-2693(83)91605-2).
- 1204 [22] G. BATTAGLIA et al., *Erratum: The radial velocity dispersion profile of the Galactic halo:  
 1205 constraining the density profile of the dark halo of the Milky Way*, Mon. Not. R. Astron.  
 1206 Soc. 370.2 (Aug. 2006), pp. 1055–1056, DOI: 10.1111/j.1365-2966.2006.10688.x.
- 1207 [23] G. BATTAGLIA et al., *The radial velocity dispersion profile of the Galactic halo: constrain-  
 1208 ing the density profile of the dark halo of the Milky Way*, Mon. Not. R. Astron. Soc.  
 1209 364.2 (Dec. 2005), pp. 433–442, DOI: 10.1111/j.1365-2966.2005.09367.x,  
 1210 arXiv: astro-ph/0506102 [astro-ph].
- 1211 [24] G. L. BAYATYAN et al., *CMS TriDAS project: Technical Design Report, Volume 1: The  
 1212 Trigger Systems*, Technical Design Report CMS.
- 1213 [25] C. M. BENDER and S. SARKAR, *Asymptotic Analysis of the Boltzmann Equation for  
 1214 Dark Matter Relics*, J. Math. Phys. 53 (2012), p. 103509, DOI: 10.1063/1.4753990,  
 1215 arXiv: 1203.1822 [hep-th].
- 1216 [26] M. BENEDIKT, D. SCHULTE and F. ZIMMERMANN, *Optimizing integrated luminosity  
 1217 of future hadron colliders*, Phys. Rev. Spec. Top. Accel. Beams 18.CERN-ACC-2015-  
 1218 0166. 10 (Oct. 2015), 101002. 19 p, DOI: 10.1103/PhysRevSTAB.18.101002.
- 1219 [27] P. BEVINGTON and D. ROBINSON, *Data Reduction and Error Analysis for the Physical  
 1220 Sciences*, McGraw-Hill Higher Education, McGraw-Hill Education, 2003, ISBN:  
 1221 9780072472271.
- 1222 [28] P. BHATTACHARJEE et al., *Sizing-up the WIMPs of Milky Way : Deriving the velocity  
 1223 distribution of Galactic Dark Matter particles from the rotation curve data*, Phys. Rev.  
 1224 D87 (2013), p. 083525, DOI: 10.1103/PhysRevD.87.083525, arXiv: 1210.2328  
 1225 [astro-ph.GA].

## BIBLIOGRAPHY

---

- 1228 [29] P. BLOCH et al., *Changes to CMS ECAL electronics: addendum to the Technical Design*  
1229 *Report*, Technical Design Report CMS, CERN, Geneva, 2002.
- 1230 [30] A. BOVEIA and C. DOGLIONI, *Dark Matter Searches at Colliders*, Ann. Rev. Nucl.  
1231 Part. Sci. 68 (2018), pp. 429–459, doi: 10.1146/annurev-nucl-101917-021008,  
1232 arXiv: 1810.12238 [hep-ex].
- 1233 [31] A. H. BROEILS, *The mass distribution of the dwarf spiral NGC 1560*, Astronomy &  
1234 Astrophysics 256 (Mar. 1992), pp. 19–32.
- 1235 [32] O. S. BRÜNING et al., *LHC Design Report*, CERN Yellow Reports: Monographs,  
1236 CERN, Geneva, 2004, doi: 10.5170/CERN-2004-003-V-1.
- 1237 [33] M. CACCIARI, G. P. SALAM and G. SOYEZ, *The Anti- $k(t)$  jet clustering algorithm*, JHEP  
1238 04 (2008), p. 063, doi: 10.1088/1126-6708/2008/04/063, arXiv: 0802.1189  
1239 [hep-ph].
- 1240 [34] A. CANEPA, *Searches for supersymmetry at the Large Hadron Collider*, Reviews in  
1241 Physics 4 (2019), p. 100033, ISSN: 2405-4283, doi: <https://doi.org/10.1016/j.revip.2019.100033>.
- 1243 [35] D. G. CERDEÑO et al., *B anomalies and dark matter: a complex connection*, The  
1244 European Physical Journal C 79.6 (2019), p. 517, doi: 10.1140/epjc/s10052-  
1245 019-6979-x.
- 1246 [36] S. CHATRHYAN et al., *Description and performance of track and primary-vertex recon-  
1247 struction with the CMS tracker*, JINST 9.10 (2014), P10009, doi: 10.1088/1748-  
1248 0221/9/10/P10009, arXiv: 1405.6569 [physics.ins-det].
- 1249 [37] S. CHATRHYAN et al., *Observation of a New Boson at a Mass of 125 GeV with the  
1250 CMS Experiment at the LHC*, Phys. Lett. B716 (2012), pp. 30–61, doi: 10.1016/j.  
1251 physletb.2012.08.021, arXiv: 1207.7235 [hep-ex].
- 1252 [38] S. CITTOLIN, A. RÁCZ and P. SPHICAS, *CMS The TriDAS Project: Technical Design  
1253 Report, Volume 2: Data Acquisition and High-Level Trigger. CMS trigger and data-  
1254 acquisition project*, Technical Design Report CMS, CERN, Geneva, 2002.
- 1255 [39] D. CLOWE, A. GONZALEZ and M. MARKEVITCH, *Weak-Lensing Mass Reconstruction of  
1256 the Interacting Cluster 1E 0657-558: Direct Evidence for the Existence of Dark Matter*,  
1257 The Astrophysical Journal 604.2 (2004), p. 596.
- 1258 [40] T. COHEN, M. LISANTI and H. K. LOU, *Semi-visible Jets: Dark Matter Undercover at  
1259 the LHC*, Phys. Rev. Lett. 115.17 (2015), p. 171804, doi: 10.1103/PhysRevLett.  
1260 115.171804, arXiv: 1503.00009 [hep-ph].

- 1261 [41] T. COHEN et al., *LHC Searches for Dark Sector Showers*, JHEP 11 (2017), p. 196, doi:  
1262 10.1007/JHEP11(2017)196, arXiv: 1707.05326 [hep-ph].
- 1263 [42] C. COLLABORATION, *CMS Luminosity Public Results*, URL: <https://twiki.cern.ch/twiki/bin/view/CMSPublic/LumiPublicResults> (visited on 22/02/2020).
- 1264 [43] C. COLLABORATION, *Luminosity Physics Object Group (Lumi POG)*, access may be  
1265 restricted, URL: <https://twiki.cern.ch/twiki/bin/viewauth/CMS/TWikiLUM>  
1266 (visited on 16/03/2020).
- 1267 [44] C. COLLABORATION, *Particle-Flow Event Reconstruction in CMS and Performance for  
1268 Jets, Taus, and MET*, tech. rep. CMS-PAS-PFT-09-001, CERN, Geneva, Apr. 2009.
- 1269 [45] C. COLLABORATION, *The CMS electromagnetic calorimeter project: Technical Design  
1270 Report*, Technical Design Report CMS, CERN, Geneva, 1997.
- 1271 [46] C. COLLABORATION, *The CMS hadron calorimeter project: Technical Design Report*,  
1272 Technical Design Report CMS, CERN, Geneva, 1997.
- 1273 [47] C. COLLABORATION, *The CMS magnet project: Technical Design Report*, Technical  
1274 Design Report CMS, CERN, Geneva, 1997.
- 1275 [48] C. COLLABORATION, *The CMS tracker: addendum to the Technical Design Report*, Tech-  
1276 nical Design Report CMS, CERN, Geneva, 2000.
- 1277 [49] J. CONRAD and O. REIMER, *Indirect dark matter searches in gamma and cosmic rays*,  
1278 Nature Phys. 13.3 (2017), pp. 224–231, doi: 10.1038/nphys4049, arXiv: 1705.  
1279 11165 [astro-ph.HE].
- 1280 [50] B. COX and J. FORSHAW, *Universal: A Journey Through the Cosmos*, Penguin Books  
1281 Limited, 2016, ISBN: 9780141968346.
- 1282 [51] M. DELLA NEGRA et al., *CMS: letter of intent by the CMS Collaboration for a general  
1283 purpose detector at LHC*, tech. rep. CERN-LHCC-92-003. LHCC-I-1, Open present-  
1284 ation to the LHCC 5 November 1992, M. Della Negra/CERN, CMS Spokesman,  
1285 CERN, Geneva, 1992.
- 1286 [52] N. DEV et al., *The CMS Level-1 electron and photon trigger: for Run II of LHC*, Journal  
1287 of Instrumentation 12.02 (Feb. 2017), pp. C02014–C02014, doi: 10.1088/1748-  
1288 0221/12/02/c02014.
- 1289 [53] A. DJOUADI et al., *Direct Detection of Higgs-Portal Dark Matter at the LHC*, Eur.  
1290 Phys. J. C73.6 (2013), p. 2455, doi: 10.1140/epjc/s10052-013-2455-1, arXiv:  
1291 1205.3169 [hep-ph].
- 1292

## BIBLIOGRAPHY

---

- 1293 [54] M. DREWES, *The Phenomenology of Right Handed Neutrinos*, International Journal  
1294 of Modern Physics E 22.08 (2013), p. 1330019, doi: 10.1142/S0218301313300191.
- 1295 [55] J. EINASTO, *Dark Matter*, ArXiv e-prints (Jan. 2009), arXiv: 0901.0632 [astro-ph.CO].
- 1296 [56] F. ENGLERT and R. BROUT, *Broken Symmetry and the Mass of Gauge Vector Mesons*,  
1297 Phys. Rev. Lett. 13 (9 Aug. 1964), pp. 321–323, doi: 10.1103/PhysRevLett.13.  
1298 321.
- 1299 [57] V. FANTI et al., *A new measurement of direct CP violation in two pion decays of the*  
1300 *neutral kaon*, Physics Letters B 465.1-4 (Oct. 1999), pp. 335–348, issn: 0370-2693,  
1301 doi: 10.1016/s0370-2693(99)01030-8.
- 1302 [58] M. FARINA, M. PERELSTEIN and N. REY-LE LORIER, *Higgs Couplings and Naturalness*,  
1303 Phys. Rev. D90.1 (2014), p. 015014, doi: 10.1103/PhysRevD.90.015014, arXiv:  
1304 1305.6068 [hep-ph].
- 1305 [59] B. D. FIELDS et al., *Big-Bang Nucleosynthesis After Planck*, JCAP 2003.03 (2020),  
1306 p. 010, doi: 10.1088/1475-7516/2020/03/010, arXiv: 1912.01132 [astro-ph.CO].
- 1307 [60] C. FINANCE and A. P. DEPARTMENT, *2020 Annual Contributions to CERN budget*,  
1308 URL: <https://fap-dep.web.cern.ch/rpc/2020-annual-contributions-cern-budget> (visited on 30/03/2020).
- 1310 [61] K. C. FREEMAN, *On the Disks of Spiral and S0 Galaxies*, The Astrophysical Journal  
1311 160 (June 1970), p. 811, doi: 10.1086/150474.
- 1312 [62] S. FRIXIONE, P. NASON and C. OLEARI, *Matching NLO QCD computations with*  
1313 *Parton Shower simulations: the POWHEG method*, JHEP 11 (2007), p. 070, doi:  
1314 10.1088/1126-6708/2007/11/070, arXiv: 0709.2092 [hep-ph].
- 1315 [63] P. GONDOLO and G. GELMINI, *Cosmic Abundances of Stable Particles: improved ana-*  
1316 *lysis*, Nuclear Physics B - NUCL PHYS B 360 (Aug. 1991), pp. 145–179, doi:  
1317 10.1016/0550-3213(91)90438-4.
- 1318 [64] G. S. GURALNIK, C. R. HAGEN and T. W. B. KIBBLE, *Global Conservation Laws and*  
1319 *Massless Particles*, Phys. Rev. Lett. 13 (20 Nov. 1964), pp. 585–587, doi: 10.1103/  
1320 PhysRevLett.13.585.
- 1321 [65] L. J. HALL et al., *Freeze-In Production of FIMP Dark Matter*, JHEP 03 (2010), p. 080,  
1322 doi: 10.1007/JHEP03(2010)080, arXiv: 0911.1120 [hep-ph].
- 1323 [66] T. HAN, Z. LIU and A. NATARAJAN, *Dark matter and Higgs bosons in the MSSM*, JHEP  
1324 11 (2013), p. 008, doi: 10.1007/JHEP11(2013)008, arXiv: 1303.3040 [hep-ph].

- 1325 [67] T. HAN, J. D. LYKKEN and R.-J. ZHANG, *On Kaluza-Klein states from large extra*  
 1326 *dimensions*, Phys. Rev. D59 (1999), p. 105006, DOI: 10.1103/PhysRevD.59.105006,  
 1327 arXiv: hep-ph/9811350 [hep-ph].
- 1328 [68] F. HASERT et al., *Observation of neutrino-like interactions without muon or electron*  
 1329 *in the gargamelle neutrino experiment*, Physics Letters B 46.1 (1973), pp. 138–140,  
 1330 ISSN: 0370-2693, DOI: [https://doi.org/10.1016/0370-2693\(73\)90499-1](https://doi.org/10.1016/0370-2693(73)90499-1).
- 1331 [69] F. HASERT et al., *Search for elastic muon-neutrino electron scattering*, Physics Letters B  
 1332 46.1 (1973), pp. 121–124, ISSN: 0370-2693, DOI: [https://doi.org/10.1016/0370-2693\(73\)90494-2](https://doi.org/10.1016/0370-2693(73)90494-2).
- 1334 [70] S. HEINEMEYER et al., *Handbook of LHC Higgs Cross Sections: 3. Higgs Properties:*  
 1335 *Report of the LHC Higgs Cross Section Working Group*, ed. by S. HEINEMEYER, CERN  
 1336 Yellow Reports: Monographs, July 2013.
- 1337 [71] W. HERR and B. MURATORI, *Concept of luminosity* (2006), DOI: 10.5170/CERN-  
 1338 2006-002.361.
- 1339 [72] J. HERZOG-ARBEITMAN et al., *Empirical Determination of Dark Matter Velocities us-*  
 1340 *ing Metal-Poor Stars*, Phys. Rev. Lett. 120.4 (2018), p. 041102, DOI: 10.1103/  
 1341 PhysRevLett.120.041102, arXiv: 1704.04499 [astro-ph.GA].
- 1342 [73] P. W. HIGGS, *Broken Symmetries and the Masses of Gauge Bosons*, Phys. Rev. Lett. 13  
 1343 (16 Oct. 1964), pp. 508–509, DOI: 10.1103/PhysRevLett.13.508.
- 1344 [74] D. HUTERER, *Weak lensing, dark matter and dark energy*, General Relativity and  
 1345 Gravitation 42 (Sept. 2010), pp. 2177–2195, DOI: 10.1007/s10714-010-1051-z,  
 1346 arXiv: 1001.1758 [astro-ph.CO].
- 1347 [75] P. R. KAFLE et al., *On the Shoulders of Giants: Properties of the Stellar Halo and the*  
 1348 *Milky Way Mass Distribution*, Astrophys. J. 794.1 (2014), p. 59, DOI: 10.1088/0004-  
 1349 637X/794/1/59, arXiv: 1408.1787 [astro-ph.GA].
- 1350 [76] M. KAKIZAKI et al., *Phenomenological constraints on light mixed sneutrino dark matter*  
 1351 *scenarios*, Physics Letters B 749 (2015), pp. 44–49, ISSN: 0370-2693, DOI: <https://doi.org/10.1016/j.physletb.2015.07.030>.
- 1353 [77] J. C. KAPTEYN, *First Attempt at a Theory of the Arrangement and Motion of the Sidereal*  
 1354 *System*, The Astrophysical Journal 55 (May 1922), p. 302, DOI: 10.1086/142670.
- 1355 [78] V. KARIMÄKI et al., *The CMS tracker system project: Technical Design Report*, Technical  
 1356 Design Report CMS, CERN, Geneva, 1997.

## BIBLIOGRAPHY

---

- 1357 [79] V. KHACHATRYAN et al., *A search for new phenomena in  $pp$  collisions at  $\sqrt{s} = 13$  TeV in*  
1358 *final states with missing transverse momentum and at least one jet using the  $\alpha_T$  variable*,  
1359 *Eur. Phys. J. C77.5* (2017), p. 294, DOI: 10.1140/epjc/s10052-017-4787-8,  
1360 arXiv: 1611.00338 [hep-ex].
- 1361 [80] V. KHACHATRYAN et al., *Search for dark matter, extra dimensions, and unparticles in*  
1362 *monojet events in proton–proton collisions at  $\sqrt{s} = 8$  TeV*, *Eur. Phys. J. C75.5* (2015),  
1363 p. 235, DOI: 10.1140/epjc/s10052-015-3451-4, arXiv: 1408.3583 [hep-ex].
- 1364 [81] V. KHACHATRYAN et al., *Search for Microscopic Black Hole Signatures at the Large Had-*  
1365 *ron Collider*, *Phys. Lett. B697* (2011), pp. 434–453, DOI: 10.1016/j.physletb.  
1366 2011.02.032, arXiv: 1012.3375 [hep-ex].
- 1367 [82] G. KRNJAC, *Freezing In, Heating Up, and Freezing Out: Predictive Nonthermal Dark*  
1368 *Matter and Low-Mass Direct Detection*, *JHEP 10* (2018), p. 136, DOI: 10.1007/  
1369 JHEP10(2018)136, arXiv: 1711.11038 [hep-ph].
- 1370 [83] J. G. LAYTER, *The CMS muon project: Technical Design Report*, Technical Design  
1371 Report CMS, CERN, Geneva, 1997.
- 1372 [84] M. LISANTI, *Lectures on Dark Matter Physics*, in: *Proceedings, Theoretical Advanced*  
1373 *Study Institute in Elementary Particle Physics: New Frontiers in Fields and Strings (TASI*  
1374 *2015): Boulder, CO, USA, June 1-26, 2015*, 2017, pp. 399–446, DOI: 10.1142/  
1375 9789813149441\_0007, arXiv: 1603.03797 [hep-ph].
- 1376 [85] S. P. MARTIN, *A Supersymmetry primer*, *Adv. Ser. Direct. High Energy Phys* 18  
1377 (1998), pp. 1–98, DOI: 10.1142/9789812839657\_0001, 10.1142/9789814307505\_  
1378 0001, arXiv: hep-ph/9709356 [hep-ph].
- 1379 [86] S. MERTENS, *Direct Neutrino Mass Experiments*, *Journal of Physics: Conference Series*  
1380 718.2 (2016), p. 022013.
- 1381 [87] J. MOUSA et al., *Overview of the CMS Detector Performance at LHC Run 2*, *Universe*  
1382 5 (Jan. 2019), p. 18.
- 1383 [88] K. NAKAMURA and P. D. GROUP, *Review of Particle Physics*, *Journal of Physics G: Nuclear and Particle Physics* 37.7A (2010), p. 075021.
- 1385 [89] P. NASON, *A New method for combining NLO QCD with shower Monte Carlo al-*  
1386 *gorithms*, *JHEP 11* (2004), p. 040, DOI: 10.1088/1126-6708/2004/11/040, arXiv:  
1387 hep-ph/0409146 [hep-ph].

- 1388 [90] M. PERSIC, P. SALUCCI and F. STEL, *The universal rotation curve of spiral galaxies - I.*  
 1389 *The dark matter connection*, Mon. Not. R. Astron. Soc. 281 (July 1996), pp. 27–47,  
 1390 DOI: 10.1093/mnras/281.1.27, eprint: astro-ph/9506004.
- 1391 [91] T. SAKUMA, *Cutaway diagrams of CMS detector* (May 2019).
- 1392 [92] M. SCHUMANN, *Direct Detection of WIMP Dark Matter: Concepts and Status*, J. Phys.  
 1393 G46.10 (2019), p. 103003, DOI: 10.1088/1361-6471/ab2ea5, arXiv: 1903.03026  
 1394 [astro-ph.CO].
- 1395 [93] A. M. SIRUNYAN et al., *Observation of Higgs boson decay to bottom quarks*, Phys. Rev.  
 1396 Lett. 121.12 (2018), p. 121801, DOI: 10.1103/PhysRevLett.121.121801, arXiv:  
 1397 1808.08242 [hep-ex].
- 1398 [94] A. M. SIRUNYAN et al., *Particleflow reconstruction and global event description with the*  
 1399 *CMS detector*, JINST 12 (2017), P10003, DOI: 10.1088/1748-0221/12/10/P10003,  
 1400 arXiv: 1706.04965 [physics.ins-det].
- 1401 [95] A. M. SIRUNYAN et al., *Search for natural and split supersymmetry in proton-proton*  
 1402 *collisions at  $\sqrt{s} = 13 \text{ TeV}$  in final states with jets and missing transverse momentum*,  
 1403 Journal of High Energy Physics 2018.5 (May 2018), p. 25, DOI: 10.1007/JHEP05(2018)■
- 1404 025.
- 1405 [96] A. M. SIRUNYAN et al., *Search for dijet resonances in proton–proton collisions at  $\sqrt{s}$*   
 1406 *= 13 \text{ TeV}* *and constraints on dark matter and other models*, Phys. Lett. B769 (2017),  
 1407 [Erratum: Phys. Lett.B772,882(2017)], pp. 520–542, DOI: 10.1016/j.physletb.  
 1408 2017.09.029, 10.1016/j.physletb.2017.02.012, arXiv: 1611.03568  
 1409 [hep-ex].
- 1410 [97] A. M. SIRUNYAN et al., *Search for invisible decays of a Higgs boson produced through*  
 1411 *vector boson fusion in proton-proton collisions at  $\sqrt{s} = 13 \text{ TeV}$*  (2018), arXiv: 1809.  
 1412 05937 [hep-ex].
- 1413 [98] A. M. SIRUNYAN et al., *Search for new particles decaying to a jet and an emerging jet*,  
 1414 JHEP 02 (2019), p. 179, DOI: 10.1007/JHEP02(2019)179, arXiv: 1810.10069  
 1415 [hep-ex].
- 1416 [99] T. SJÖSTRAND et al., *An Introduction to PYTHIA 8.2*, Comput. Phys. Commun. 191  
 1417 (2015), pp. 159–177, DOI: 10.1016/j.cpc.2015.01.024, arXiv: 1410.3012  
 1418 [hep-ph].
- 1419 [100] A. SOPCZAK, *Precision Measurements in the Higgs Sector at ATLAS and CMS*, PoS  
 1420 FFK2019.arXiv:2001.05927 (Jan. 2020), 006. 9 p, DOI: 10.22323/1.353.0006.

## BIBLIOGRAPHY

---

- 1421 [101] M. J. STRASSLER and K. M. ZUREK, *Echoes of a hidden valley at hadron colliders*, Phys.  
1422 Lett. B651 (2007), pp. 374–379, doi: 10.1016/j.physletb.2007.06.055, arXiv:  
1423 hep-ph/0604261 [hep-ph].
- 1424 [102] L. G. TRENTADUE et al., *Neutrino counting*, CERN-TH-5528-89 (Sept. 1989), 42 p,  
1425 doi: 10.5170/CERN-1989-008-V-1.129.
- 1426 [103] A. VICENTE, *Anomalies in  $b \rightarrow s$  transitions and dark matter*, Advances in High  
1427 Energy Physics 2018 (Mar. 2018), doi: 10.1155/2018/3905848.
- 1428 [104] S. WEINBERG, *Cosmology*, Cosmology, OUP Oxford, 2008, ISBN: 9780191523601.
- 1429 [105] S. D. M. WHITE and M. J. REES, *Core condensation in heavy halos: a two-stage theory  
1430 for galaxy formation and clustering*, Mon. Not. R. Astron. Soc. 183.3 (1978), p. 341,  
1431 doi: 10.1093/mnras/183.3.341.
- 1432 [106] C. YOZIN and K. BEKKI, *The quenching and survival of ultra-diffuse galaxies in the  
1433 Coma cluster*, Mon. Not. R. Astron. Soc. 452.1 (2015), pp. 937–943, doi: 10.1093/  
1434 mnras/stv1073, arXiv: 1507.05161 [astro-ph.GA].
- 1435 [107] A. ZABI et al., *The CMS Level-1 Calorimeter Trigger for the LHC Run II*, Journal  
1436 of Instrumentation 12.01 (Jan. 2017), pp. C01065–C01065, doi: 10.1088/1748-  
1437 0221/12/01/c01065.

## GLOSSARY

- 1439 ***b*-jet** A jet identified by a given algorithm or classifier as originating from a *b* quark.
- 1440 **PARTICLE FLOW algorithm** An event reconstruction algorithm used in CMS. Information  
1441 from all subdetectors is combined so that all stable particles can be identified. Jets are  
1442 clustered, and complex objects such as *b*-jets are classified.
- 1443 **anti- $k_T$  algorithm** A sequential clustering algorithm designed to group hadronic particles  
1444 into jets with a radius parameter ( $R$ ). The transverse momentum is symbolised as  $k_T$   
1445 instead of  $p_T$ . In CMS, standard radius parameters are  $R = 0.4$  and  $R = 0.8$ , referred  
1446 to as AK4 and AK8 jets, respectively.
- 1447 **control region** A region of phase space orthogonal to the signal region, typically by requir-  
1448 ing an object that would otherwise be vetoed in the signal region. A control region  
1449 enriched in a background process present in the signal region (such as  $W(\rightarrow \ell\nu) + \text{jets}$ )  
1450 can be used to model its influence more accurately.
- 1451 **jet** A collimated shower of hadronic particles. High momentum quarks and gluons frag-  
1452 ment due to colour confinement; the resulting particles deposit energy in the detector  
1453 very close to each other and is reconstructed as a single physics object called a jet.
- 1454 **luminosity** Instantaneous luminosity is a measure of the collision rate in a particle accel-  
1455 erator (given in units of area per unit time). The integrated luminosity is the instant-  
1456 aneous luminosity integrated over time and is a metric for the total amount of data  
1457 delivered by an accelerator or collected by a detector.
- 1458 **missing transverse energy** The negative vector sum of the transverse momentum of all  
1459 particles in a collider event. It is sometimes abbreviate to “MET”, and also referred to  
1460 in literature as “missing transverse momentum” ( $p_T^{\text{miss}}$ ).

## GLOSSARY

---

- <sup>1461</sup> **pileup** The term ascribed to additional proton-proton collisions during a bunch crossing.  
<sup>1462</sup> Pileup interactions typically produce a large number of low-momentum particles.
- <sup>1463</sup> **semi-visible jet** A shower of standard model and dark hadrons from the decay of a leptophobic  $Z'$  or  $\Phi$  mediator that couples the hidden sector to the standard model.
- <sup>1465</sup> **sideband** A region of phase space orthogonal to the signal region, typically by inverting kinematic requirements. Similar to a control region, a sideband enriched in a background present in the signal region (such as QCD) can be used to model it more accurately.  
<sup>1466</sup>  
<sup>1467</sup>

1469 **eV** electron volt.

1470 **CMSSW** CMS SoftWare.

1471 **AEGIS** Antihydrogen Experiment: Gravity, Interferometry, Spectroscopy.

1472 **ALICE** A Large Ion Collider Experiment.

1473 **ATLAS** A Toroidal LHC ApparatuS.

1474 **BSM** beyond the standard model.

1475 **CERN** *Organisation Européenne pour la Recherche Nucléaire* (European Organisation for  
1476 Nuclear Research).

1477 **CMS** Compact Muon Solenoid.

1478 **DAQ** data acquisition.

1479 **ECAL** electromagnetic calorimeter.

1480 **FASER** ForwArd Search ExpeRiment.

1481 **FCC** Future Circular Collider.

1482 **HCAL** hadron calorimeter.

1483 **HF** hadron forward calorimeter.

1484 **HL-LHC** High Luminosity Large Hadron Collider.

1485 **HLT** High-Level Trigger.

## ACRONYMS

---

1486 **ISOLDE** Isotope Separator On Line DEvice.

1487 **JEC** jet energy corrections.

1488 **L1** Level-1.

1489 **L1T** Level-1 Trigger.

1490 **LEP** Large Electron-Positron Collider.

1491 **LHC** Large Hadron Collider.

1492 **LO** leading order.

1493 **LSP** lightest supersymmetric particle.

1494 **LZ** LUX-ZEPLIN.

1495 **MC** Monte Carlo.

1496 **MoEDAL** Monopole and Exotics Detector at the LHC.

1497 **MOND** modified Newtonian dynamics.

1498 **PF** Particle Flow.

1499 **PS** Proton Synchrotron.

1500 **PSB** Proton Synchrotron Booster.

1501 **QCD** Quantum Chromodynamics.

1502 **SM** standard model.

1503 **SPS** Super Proton Synchrotron.

1504 **SUSY** supersymmetry.

1505 **TOTEM** TOTal Elastic and diffractive cross section Measurement.

1506 **VBF** vector boson fusion.

1507 **WIMP** Weakly Interacting Massive Particle.